


RESEARCH ARTICLE

Open Access



Molecular hydrogen promotes wound healing by inducing early epidermal stem cell proliferation and extracellular matrix deposition

Pengxiang Zhao^{1,2,3}, Zheng Dang^{1,2,3}, Mengyu Liu^{1,2,3}, Dazhi Guo⁴, Ruiliu Luo^{1,2,3}, Mingzi Zhang⁵, Fei Xie^{1,2,3}, Xujuan Zhang^{1,2,3}, Youbin Wang⁵, Shuyi Pan⁴ and Xuemei Ma^{1,2,3*} 

Abstract

Background Despite progress in developing wound care strategies, there is currently no treatment that promotes the self-tissue repair capabilities. H₂ has been shown to effectively protect cells and tissues from oxidative and inflammatory damage. While comprehensive effects and how H₂ functions in wound healing remains unknown, especially for the link between H₂ and extracellular matrix (ECM) deposition and epidermal stem cells (EpSCs) activation.

Methods Here, we established a cutaneous aseptic wound model and applied a high concentration of H₂ (66% H₂) in a treatment chamber. Molecular mechanisms and the effects of healing were evaluated by gene functional enrichment analysis, digital spatial profiler analysis, blood perfusion/oxygen detection assay, in vitro tube formation assay, enzyme-linked immunosorbent assay, immunofluorescent staining, non-targeted metabolomic analysis, flow cytometry, transmission electron microscope, and live-cell imaging.

Results We revealed that a high concentration of H₂ (66% H₂) greatly increased the healing rate (3 times higher than the control group) on day 11 post-wounding. The effect was not dependent on O₂ or anti-reactive oxygen species functions. Histological and cellular experiments proved the fast re-epithelialization in the H₂ group. ECM components early (3 days post-wounding) deposition were found in the H₂ group of the proximal wound, especially for the dermal col-I, epidermal col-III, and dermis-epidermis-junction col-XVII. H₂ accelerated early autologous EpSCs proliferation (1–2 days in advance) and then differentiation into myoepithelial cells. These epidermal myoepithelial cells could further contribute to ECM deposition. Other beneficial outcomes include sustained moist healing, greater vascularization, less T-helper-1 and T-helper-17 cell-related systemic inflammation, and better tissue remodelling.

Conclusion We have discovered a novel pattern of wound healing induced by molecular hydrogen treatment. This is the first time to reveal the direct link between H₂ and ECM deposition and EpSCs activation. These H₂-induced multiple advantages in healing may be related to the enhancement of cell viability in various cells and the maintenance of mitochondrial functions at a basic level in the biological processes of life.

Keywords Molecular hydrogen, Wound care, Extracellular matrix deposition, Epidermal stem cell proliferation, Re-epithelialization

*Correspondence:

Xuemei Ma

xmma@bjut.edu.cn

Full list of author information is available at the end of the article



© The Author(s) 2023. **Open Access** This article is licensed under a Creative Commons Attribution 4.0 International License, which permits use, sharing, adaptation, distribution and reproduction in any medium or format, as long as you give appropriate credit to the original author(s) and the source, provide a link to the Creative Commons licence, and indicate if changes were made. The images or other third party material in this article are included in the article's Creative Commons licence, unless indicated otherwise in a credit line to the material. If material is not included in the article's Creative Commons licence and your intended use is not permitted by statutory regulation or exceeds the permitted use, you will need to obtain permission directly from the copyright holder. To view a copy of this licence, visit <http://creativecommons.org/licenses/by/4.0/>.

Introduction

Wound healing in adult mammals generally involves four major processes [1–4]: haemostasis, inflammation, proliferation, and remodelling—which may leave a scar [5, 6]. Failure at any of these stages could lead to acute or chronic wound repair disorders [7]. In evaluating wound healing, the acronym “TIME” (Tissue, Infection/Inflammation, Moisture balance, and Edge of wound) has been used to describe a favourable wound-bed microenvironment [8, 9]. Throughout the dynamic healing process, rapid re-epithelialization is mediated by epidermal stem cells (EpSCs) and the extracellular matrix (ECM) to restore the skin barrier [10–12]. EPSCs can be activated and recruited from various tissues [13], such as hair follicles (HFs), interfollicular epidermis (IFE), and bone marrow [14–17], thus replenishing the keratinocytes at the wound site and facilitating wound closure [18, 19]. Furthermore, ECM molecules can stimulate keratinocyte migration from the edges of the wound and nearby tissues to the wound bed [20, 21]. In addition to serving as a scaffold [22], the ECM is instrumental in creating a favourable environment for skin progenitor cells [23]. This is largely due to collagen in the ECM [24], which is synthesized by fibroblasts, epithelial cells [25], and keratinocytes [12], and constitutes a basis for translational wound-repair medications and therapies [26–29]. However, the process of healing is multifaceted, and improvements in wound healing, including safer and more efficient wound-healing methods, are needed.

Wound healing processes involve the spatial and temporal synchronization of a variety of cell types with distinct roles in all phases [30]. During these, the reactive oxygen species (ROS) gradient is considered as one of the first signals that activate the cellular response and also crucial to regulate several other phases of healing processes [31]. While key factors that promote wound healing also include avoiding the tissue damage caused by the overproduction of ROS and activating the functions of tissue repair.

Hydrogen gas has been reported by Ohsawa et al. [32] in 2007 to be an efficient antioxidant in protecting rats brain from ischemia-reperfusion injury. Other studies added evidence of H₂ therapy in massive oxidative damage and inflammatory diseases [33–36]. Latest researches suggest that hydrogen can also be beneficial on skin injury, for example, H₂ has been shown to effectively improve the damage repair of cutaneous wound [37], burn wound [38], pressure ulcer [39, 40], diabetic wounds [41, 42], radiation injury [43], psoriasis damage [44], and oral-wound [45]. Current explanations for hydrogen promoting wound healing have been mostly focused on its ability of anti-inflammatory, anti-oxidative stress and reacting with cytotoxic ROS. Few studies indicated that H₂ may function in stem cell viability

and collagen synthesis. Kawasaki et al. [46] suggested hydrogen gas prolonged replicative lifespan of bone marrow cells in vitro, and Zhang et al. [47] pointed out that hydrogen protected hematopoietic stem cell from radiation injury by reducing hydroxyl radical. In a study of pressure ulcer, masson staining was used to prove hydrogen inhalation induced collagen synthesis [40], another study of diabetic wound, topical application of H₂ was revealed to induce Col-1 [42]. More comprehensive and deep research of hydrogen on wound healing are still needed, and many questions remains to be answered, such as how H₂ functions on different types of cells especially on stem cells activities? What types of collagens and other ECM are synthesized under H₂ treatment? Is this hydrogen-promoted wound healing dose-dependent?

In the present study, by using a full-thickness dorsal-skin defect mouse model, we revealed that daily treatment in an high concentration H₂ (66% H₂ + 33% O₂) chamber induced a novel pattern of wound healing with less inflammation and better angiogenesis, faster cell migration, mitochondrial function maintenance, and less scab formation. H₂ treatment facilitated early ECM deposition and EpSCs activation, thus providing a simple and effective approach to improve wound healing (mainly due to the high concentration of H₂). H₂-releasing dressing received a relevant effect in cutaneous wound healing. Therefore, H₂ treatment may potentially provide a novel strategy different from the traditional pattern of wound care, with a vast range of applications in clinical postoperative treatment.

Methods

Cell culture

Human embryonic skin fibroblasts CCC-ESF-1 (ESF) (generation 10, G10), human embryonic lung fibroblast CCC-HPF-1 (HPF) (G10), human immortal keratinocyte line (HaCaT) (G8), and human Umbilical Vein Endothelial Cells (HUVECs) (G3) were obtained from the National Infrastructure of Cell Line Resource Center, Beijing, China. Primary mesenchymal stem cells derived from newborn umbilical cords (Human Umbilical Cord Primary Mesenchymal Stem Cells (HUCP-MSCs)) were donated by Beijing Obstetrics and Gynecology Hospital. Cells were routinely cultured at 5% CO₂ and 37 °C in DMEM medium (for ESF, HPE, HaCaT, and HUVEC) (Gibco, NY, USA) supplemented with 10% fetal calf serum (Gibco, NY, USA) and 1% penicillin and streptomycin (Gibco, NY, USA).

Animal experiments

All animal studies were carried out according to protocols approved by the Committee on Ethics of Biomedicine Research, the Sixth Medical Center, PLAGH, China, and all procedures were conducted in accordance with the Regulations for the Administration of Affairs Concerning

Experimental Animals (China). Male C57BL/6J mice (7 weeks old, 20–24 g) were purchased from Vital River Laboratory Animal Technology Co., Ltd. (Beijing, China). Animals were maintained under standard conditions at 22 °C to 25 °C with a 12-h light/dark cycle and were fed a normal diet. Oral enrofloxacin (0.17 mg/mL) intake was administered in daily drinking water, and the antibiotic was prepared with chlorinate-free and acid-free water. For the NAC treatment group, 3.3 mg NAC (the ROS scavenger acetylcysteine; #S1623, Selleckchem, China) in 260 μ L distilled water was injected in each mouse with 22 (\pm 2) g of body weight.

Full-thickness cutaneous wound healing model

The full-thickness cutaneous wound healing model was established according to the Murine Model of Wound Healing [48] with some modifications (Fig. 1A). Briefly, mice were anesthetized with tribromoethyl alcohol (20 mg/mL, 10 μ L/g injection), and the hair was shaved and cleaned with 70% ethanol. We split the back skin with a ring of medical silica gel membrane (to prevent the wound closure due to loose skin of mice), and then seamed it well with medical thread and removed the center skin to create 10 mm full-thickness excisional dorsal skin wounds using a sterile scissor. Wound areas were calculated using ImageJ software, and the wound closure percentage was obtained as follows:

$$\text{Wound closure percentage (\%)} = \frac{\text{wound area on day 0} - \text{wound area on day n}}{\text{wound area on day 0}} \times 100\%$$

(See figure on next page.)

Fig. 1 Persistent high concentration of H₂ significantly accelerated cutaneous wound healing, blood perfusion and vessel formation. **A** Left: connection between each module in the H₂ chamber system. Middle: Model of the full-thickness cutaneous wound in mouse backs; inside circle = original wound, outside circle = sampling boundary. Right: Scheme of a wound section after injury. **B** Timeline of animal experiments and daily H₂ treatment (or under other conditions). Mice underwent surgery for 30 min and then immediately put in H₂ chamber for 1 h. Thereafter, they were treated with H₂ (or other conditions) every 24 h for 1 h until sacrifice. **C** Capture of wound area every two days after modeling in different persistent conditions ($n = 5$ for each group). **D** Comparison of wound closure percentage after modeling (persistent daily treatments). **E** H&E staining and Masson staining showing the tissue remodeling 11 days post-wounding (persistent daily treatments). **F** Treatment was applied for the first 3 days only, and the images of wound areas were captured every 2 days after modeling (days 0–9). **G** Comparison of wound closure percentage after modeling among the five groups (treatment for the first 3 days). **H** Blood flow perfusion 0–11 days post-wounding in the 66% H₂, 5% H₂, and Control groups. **I** Quantification of blood perfusion, SO₂, tHb, and HHb in wound area among the three groups. **J, K** Representative immunofluorescence images and quantification for CD31⁺ (green) tube formation in dermal wounds of at day 11 post-wounding. **L, M** Panoramic scanning and the quantification of wound edge tube formation at the leading edge (L, 0–1 mm from wound site), mid-end (M, 1–2 mm from wound site) and distal (D, 2–3 mm from wound site) areas of the wound at day 3 post-wounding. Yellow dotted line indicates the boundary between the epithelium and dermis. **N, O** Representative microscopic images and the quantification of in vitro blood vessel formation of Human Umbilical Vein Endothelial Cells (HUVEC) at 12 h after different treatments. Red hatched line outlines the newly formed tubes. **P** GSEA Top-5 tube formation-related GO-bp enrichment plots showed the H₂ accelerated tube formation (2 days earlier than the controls). Data in **D, G**, and **I** were analyzed by two-way ANOVA test, and data in **K, M**, and **O** were processed unpaired *t* test. All of the data are plotted as Mean \pm SEM. **P* value < 0.05; ***P* value < 0.01; ****P* value < 0.001; no stars for *P* value > 0.05; *in **D** indicates a significant difference between the 66% H₂ and control group, the 5% H₂ and control group, separately; * in **G** indicates a significant difference between the 66% H₂ and control group. Scale bar = 100 μ m. Black dotted line in **E** indicates the boundary between the epithelium and dermis. Arrow in **A** (right) indicates the epithelial tongue; black arrowheads in **E** indicate blood capillaries in the dermal layer of the wound. b, basal layer; d, dermis; he, hypertrophic epidermal wound edge; hf, hair follicles; ife, interfollicular epithelium; s, scab; sm, smooth muscle; wb, wound bed

Muscle contusion model

We developed a muscle contusion model as stated in the reference [49] to explore the role of hydrogen in muscle injury repair. Male C57/BJ mice aged 6–8 weeks were used. The detailed method is to drop a 25-g weight from a height of 60 cm to the inner surface of the gastrocnemius muscle (Figure S9A). This modeling method has moderate intensity and will not cause skeletal injury or gait abnormality.

H₂ chamber treatment

A transparent closed box (20 cm \times 18 cm \times 15 cm) was connected to a hydrogen generator (KLE-H7, Kelieng Biomedical Co. Ltd., Shenzhen, China) (Fig. 1A), which produces 66% H₂ and 33% O₂ (V/V), 5% H₂ (V/V) mixed with air, or 33% O₂ (V/V) mixed with air. Hydrogen treatment was given immediately after establishment of the mouse cutaneous wound healing establishment, and then daily administration was given until the end of the experiment. Animals were placed in the box with the mixed air for 1 h each day. During this inhalation period, mice were awake and freely moving. Thermal trace GC ultra-gas chromatography (Thermo Fisher, MA, USA) was used to monitor the concentration of hydrogen gas in the closed box.

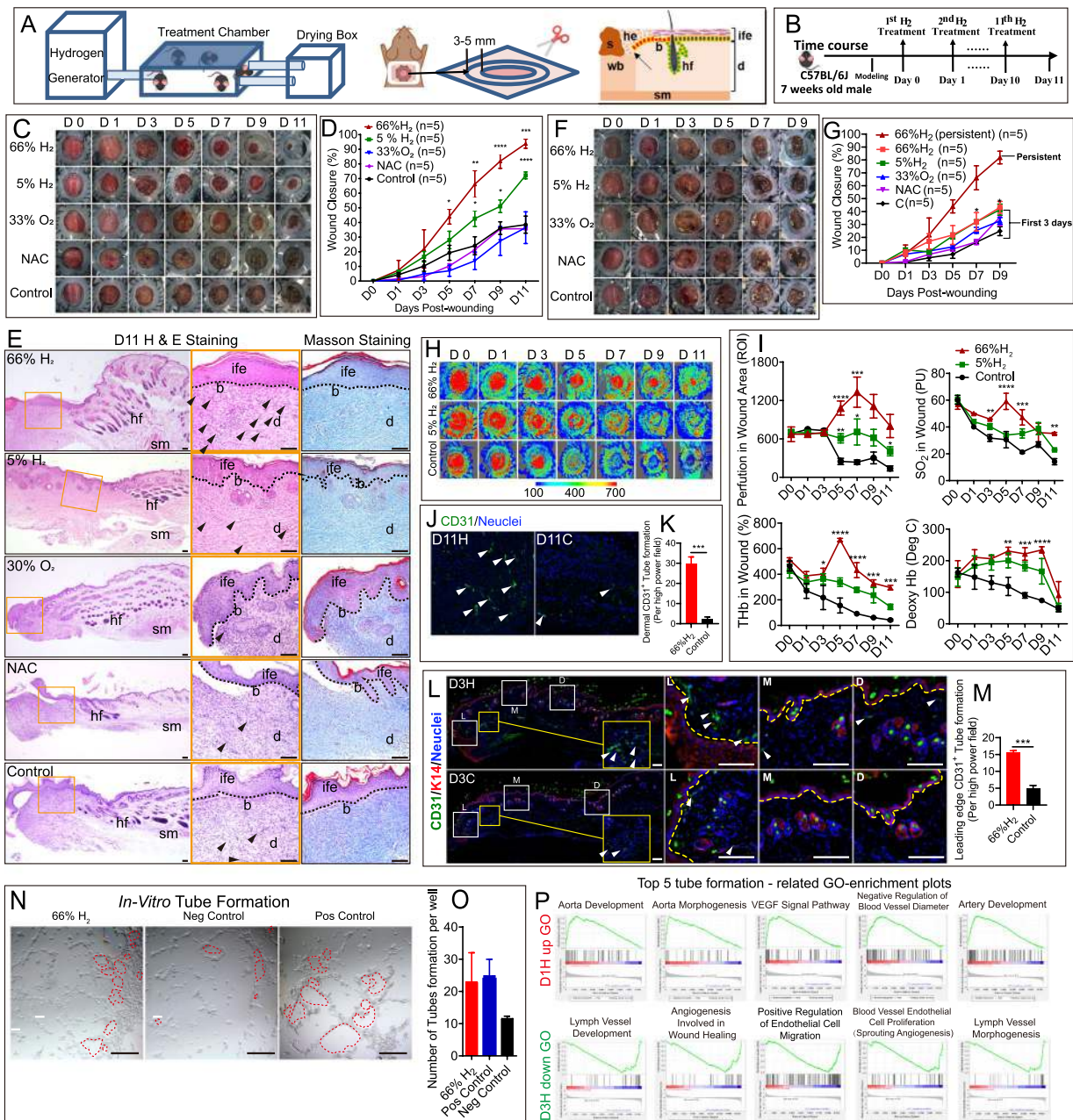


Fig. 1 (See legend on previous page.)

H₂ rich medium preparation

H₂ rich medium was produced by injecting gas using the same hydrogen generator used for H₂ Chamber treatment (KLE-H7, Kelieng Biomedical Co. Ltd., Shenzhen, China) into DMEM medium (Gibco) for 30 min hydrogen dissolved in reaction solution was detected with a needle-type H₂ sensor (Unisense, Aarhus N, Denmark). To measure the H₂ concentration in the reaction system, the sensor was inserted below the liquid surface.

Blood perfusion and blood oxygen detection

Blood perfusion at the wound site during the healing processes was detected by using a moorFLPI-2 (Moor Instruments Limited, UK) according to manufacturer instructions. Images were further selected from videos and analyzed by moorFLPIReview V50 software (Moor Instruments Limited, UK). Blood oxygen levels were tested by the moorVMS-OXY Tissue Oxygen Monitor (Moor Instruments Limited, UK) according to the

instructions. Five sites (top, bottom, left, right, and middle) of the wound area were chosen, and an average was calculated to create the oxygen kinetic curve.

In vitro tube formation assay

Tube formation assay was performed as described [50]. Firstly, Matrigel was thawed at 4 °C overnight to avoid bubble formation. Briefly, 15-well μ -Slides (ibidi, Germany) were coated with 10 μ l of Matrigel, which was allowed to solidify at 37 °C. HUVECs before generation 10 were harvested and the cell number and viability were determined by Trypan blue staining before seeding. A cell suspension was prepared in DMEM and 15,000 cells/well were seeded in 50 μ l medium on top of the matrigel. HUVECs were seeded in conditioned medium for 6 h, and the enclosed networks of complete tubes were counted and photographed under an inverted microscope. The tubular loops of the cells were measured and calculated for each well.

Digital Spatial Profiler and bulk RNA-seq analysis

Bulk RNA-seq was processed by Anoroad Inc. (Beijing, China) and the Digital Spatial Profiler assay was performed by Capital Bio Technology Inc. (Beijing, China).

Immunohistochemistry (IHC) and immunofluorescence (IF) Tissue immunostaining

Skin tissue at the wound site was harvested and fixed with formalin and embedded in paraffin blocks, and then 4 μ m thick paraffin sections were mounted on glass slides for histological staining. IHC and IF of the paraffin-embedded tissue sections were performed as previously indicated [51]. Briefly, sections were dewaxed and rehydrated by subsequent immersion in xylene, ethanol (100%, 95%, 70%, and 50%) and deionized H₂O. Antigen was then retrieved in citrate buffer, and non-specific staining between the primary antibodies (Table S1A) and the tissue was blocked by incubation in 1% goat serum in PBS for 60 min at RT. The sections were incubated with the primary antibodies listed in the Table S8A at 37 °C for 60 min for IHC or at 4 °C overnight for IF. Further labeling with specific secondary antibodies for IHC or IF (Table S1B) was performed according to the manufacturer's instructions. For IF, nuclei were stained with NucBlue Live cell stain (R37605, Invitrogen). DAB, hematoxylin and neutral balsam mounting reagent used in IHC processes were obtained from ZSGB-BIO (Beijing, China).

Cells immunofluorescence staining

Cells suspensions in a 96-well plates at 10,000 cells/well were allowed to adhere for 24 h and then switched to full medium. Wells containing the seeded cells were washed

with 1 \times PBS immediately at the end of the incubation times and fixed in 4% paraformaldehyde for 30 min. Subsequent to the fixation, the cells were permeabilized with 0.3% PBS-Tween for 15 min, washed, and then blocked with normal sheep serum blocking buffer (ZSGB-BIO, China) for at least 1 h at room temperature. Primary antibodies (Table S1A) were added at the dilution recommended by the manufacturers and were incubated overnight at 4 °C. Appropriate fluorescent dye-labeled secondary antibodies (Table S1B) were used, and cell nuclei were stained with NucBlue Live cell stain (R37605, Invitrogen).

Hematoxylin and eosin and Masson trichrome staining

The protocol described by Fischer et al was used for the Hematoxylin and eosin (H&E) staining [52], while Masson trichrome staining was performed in strict accordance with the manufacturer's protocol (Masson Stain Kit (60532ES58), Yeasen, China).

Flow cytometric staining

For analysis of Th₁, Th₂, T_{reg}, and Th₁₇ cells, single-cell suspensions were prepared from the spleens of mice 24 h after wounding. The cells were labeled with CD8-APC, CD4-FITC, and CD3-PECy5. For T-bet and GATA-3, protein amounts were normalized, and cell surface staining was performed using APC-conjugated anti-CD4 followed by fixation with 1 \times Fixation/Permeabilization buffer and intracellular staining with PE-conjugated anti-T-bet and APC-conjugated anti-GATA-3 in 1 \times permeabilization buffer. Cells were washed in 1 \times permeabilization buffer and analyzed by flow cytometry (B53009, CytoFLEX Flow Cytometer, Biotek).

For the analysis of T_{reg} cells, cell surface staining was performed using FITC-conjugated anti-CD4, PE-conjugated anti-CD25, PB450-conjugated anti-CD127 and appropriate isotype controls. Cells were incubated with antibodies for 20 min at room temperature in the dark, followed by washing in phosphate buffered solution (PBS) and analysis by flow cytometry. For the analysis of Th₁₇ cells, cells were stained with FITC anti-CD4 for surface expression of CD4, and intracellular cytokine IL-17 was detected by staining with APC-conjugated Anti-IL-17. Finally, cells were analyzed by flow cytometry. All antibodies and reagents were purchased from Biologend Inc., USA (Table S1).

For the identification of MSCs, 8 conjugated antibodies (CD73-PE, CD90-FITC, CD105-Cy5, CD34-FITC, CD45-Cy5, CD79a-PE, CD14-APC, and HLA-DR-APC-Cy7) targeting at the cell surface markers [53] were applied, and the staining and detection methods were consistent with the methods described previously.

Enzyme-linked immunosorbent assay

Murine serum was carefully collected from whole blood and stored in -80°C . Wound edge tissue was harvested after the mice were sacrificed, washed twice in distilled PBS, and cut into small pieces in lysis buffer containing protease inhibitor and 0.1 mM PMSF (Sangon Biotech, Shanghai, China), followed by homogenization and centrifugation (12,000 rpm, 20 min). The supernatant was then collected for further assessment of EGF (MM-0043M), bFGF (MM-0050M1), PDGF (MM-0070M1), and TGF- β 1 (MM-0921M) levels using mouse ELISA kits (Jiangsu Meimian industrial, China). Tissue and serum samples underwent multiple cytokines detection by using Bio-plex proTM Mouse Cytokine Th17 Panel A 6-Plex kit (#M6000007NY, Bio Rad, USA). For tissue detection, amounts of target growth factors were normalized to the total amount of whole protein.

Non-targeted metabolomics analysis

The non-targeted metabolomics analysis was performed by IGENECODE Company, Beijing, China. Thermo ScientificTM DionexTM UltiMateTM 3000 Rapid Separation LC (RSLC) system. UHPLC separation was achieved with reverse phase C18 or hydrophilic interaction liquid chromatography columns. For C18 separation, the mobile phase A was acetonitrile/water (60/40) and mobile phase B was isopropanol/ acetonitrile (90/10); both A and B contained 0.1% formic acid and 10 mmol/L ammonium acetate. The gradient conditions for reverse phase C18 separation are shown in Table S2. The HSS T3 column (2.1 \times 100 mm, 1.8 μm , waters) operated at 45 $^{\circ}\text{C}$. The flow rate was 300 $\mu\text{L}/\text{min}$, and the injection volume was 1 μL .

For HILIC separation, the mobile phase A was acetonitrile, and the mobile phase B was water; both A and B contained 0.1% formic acid and 10 mmol/L ammonium acetate. A BEH Amide column (2.1 \times 100 mm, 1.7 μm , waters) was operated at 40 $^{\circ}\text{C}$. The flow rate was 300 $\mu\text{L}/\text{min}$, and the injection volume was 1 μL (see Table S3).

A Thermo ScientificTM Q ExactiveTM hybrid quadrupole Orbitrap mass spectrometer equipped with a HESI-II probe was employed. The pos HESI-II spray voltage was 3.7 kV, the heated capillary temperature was 320 $^{\circ}\text{C}$, the sheath gas pressure was 30 psi, the auxiliary gas setting was 10 psi, and the heated vaporizer temperature was 300 $^{\circ}\text{C}$. Both the sheath gas and auxiliary gas were nitrogen. The collision gas was also nitrogen at a pressure of 1.5 mTorr. The parameters of the full mass scans were as follows: a resolution of 70,000, an auto gain control target under 1×10^6 , a maximum isolation time of 50 ms, and an m/z range 50–1500. The LC-MS system was controlled using Xcalibur 2.2 SP1.48 software (Thermo Fisher Scientific), and data were collected and processed with the same software.

All data obtained from the four assays in the two systems in both pos and neg ion modes were processed using Progenesis QI data analysis software (Nonlinear Dynamics, Newcastle, UK) for imputing raw data, peak alignment, picking, and normalization to produce peak intensities for retention time (tR) and m/z data pairs. The ranges of automatic peak picking for the C18 were between 1 and 16 min and between 1 and 12 min, respectively; adduct ions of each “feature” (m/z , tR) were deconvoluted, and these features were identified in the human metabolome database (HMDB) and Lipidmaps.

Fibroblast movement and migration and keratinocyte cell epithelialization ability test by a live cell imaging system

HPF cells were seeded at 5000 cells/well in a 96-well plate with a clear bottom, stained with Actin-GFP (C10506, CellLingt, Invitrogen, USA) and cultured for another 24 h to observe movement. ESF cells were seeded at 20,000 cells/well, scratched by the high throughput scratcher of Cytation 5 (Biotek), and then observed for another 24 h to determine the conditioned medium in fibroblast migration function. Cell movement and migration were scanned using a Cytation 5 Cell Imaging Multi-mode reader (Biotek), and migration was quantified automatically according to the manufacturer’s instructions. HaCaT cells were seeded at 30,000 cells/well and then cultured for another 24 h to observed and calculate the area of colony formation (epithelialization). The images in each small field were captured every hour in 3×3 montage frames at $\times 10$ magnification. For cell movement video footage, both bright field and fluorescent channel were used.

Preparation and evaluation of magnesium based hydrogen storage material dressing

Microparticles of magnesium (Mg) balls (average diameter 20 μm) are spread evenly on medical gauze soaked with physiological saline solution. Medical waterproof and breathable polyurethane film was covered on both sides of the medical gauze. Then the “sandwich dressing” was sealed around the edge, and sewed onto the silicone membrane at the back of the wounded animal. For the control group, normal medical gauze soaked with normal saline solution was used without Mg. All the dressings were changed every day. The release of H_2 was measured by headspace gas chromatography (GC) (Shimadzu, GCMS-QP2010S).

Statistical analysis

For comparison between two groups, two-tailed paired and unpaired Student’s t tests were performed to calculate P values and determine statistically significant differences (significance was set at $P < 0.05$, as detailed in

the figure legends). For comparison among more than two groups, ordinary one- or two-way analysis of variance (ANOVA) tests were followed by the appropriate multiple comparison tests (as detailed in the figure legends). All experiments were repeated twice with the same results. All statistical analyses were performed with GraphPad Prism 8 software.

Results

Hydrogen greatly accelerates cutaneous aseptic wound closure in full-thickness dorsal-skin defect mice

To determine whether H₂ improves wound healing, we established a cutaneous aseptic wound model using full-thickness dorsal-skin defect mice that were subjected to daily application of H₂ in a treatment chamber (Fig. 1A). Sampling region and the scheme of wound were also shown in Fig. 1A. We evaluated the effect of high (66% H₂, 66% H₂ + 33% O₂) and low (5% H₂; 5% H₂ + 21% O₂ air) concentrations of H₂ on wound healing over an 11-day time course (Fig. 1B), and included control (air) and 33% O₂ (33% O₂ in air) mouse groups for comparison. H₂ has long been recognized as an antioxidant targeting ROS; therefore, we also added an N-acetyl-L-cysteine (NAC) treatment group to evaluate a possible role of ROS cleavage in wound healing. Our results revealed that the 66% H₂ group (66% H₂ + 33% O₂) healed faster than any of the other groups. Macroscopic differences appeared on the first day after treatment and became more visible on day 3 (Fig. 1C). Eleven days after wounding, the 66% H₂ group displayed a significantly increased wound-closure rate (approximately 90% wound closure for the 66% H₂ group; as compared to 70% closure for the 5% H₂ group and about 30% closure for the control group; Fig. 1D). Furthermore, the healing rates of the NAC and 33% O₂ groups were similar to those of the control group. These results suggest that H₂ promotes healing in a dose-dependent manner, and that the healing effect is not dependent on O₂ or ROS (Fig. 1C, D).

To further visualize the effect of H₂ on wound healing, we performed histological analysis of haematoxylin and eosin (H&E) and Masson-stained sections on day 11 (Fig. 1E). The localization of the wounded skin tissue is shown in the schematic diagram (Fig. 1A, right part). The epidermis was more fully formed, and the dermal and epidermal junction (DEJ) appeared intact with more collagen deposition in the 66% H₂ group, while a weaker DEJ and partial re-epithelialization were observed in both the NAC and 33% O₂ groups. This is despite the effect of NAC in reducing EGF and TGF-β1 growth factor levels at day 3 after wounding ($p_{\text{bFGF}} < 0.01$, $p_{\text{TGF-}\beta 1} < 0.05$) (Figure S1). Thus, these results verify that neither ROS

cleavage nor 33% O₂ administration alone were able to promote the wound healing process. Notably, the wound healing pattern in the 66% H₂ group appears similar to moist healing, with less blood scab formation and better in tissue remodeling.

As the benefits of 66% H₂ application on wound healing were visible on day 3, we evaluated whether abbreviated treatment might have therapeutic value. For these experiments, we treated mice with 66% H₂ for 3 days only, and then stopped administration while continuing to monitor the mice for another 6 days. As shown in Fig. 1F, G, the 66% H₂ group healed faster than the control group; however, all healing speeds were much slower, with final wound closure rates of < 50% and blood clots visible after days 3–5. Therefore, these results suggest that persistent daily treatment is required for the full benefits of H₂.

Hydrogen increases blood flow and blood oxygen levels in the wound area and promotes early blood vessel formation

As important indicators of wound healing, the wound blood flow and blood oxygen [54, 55] content are tested to evaluate the effects of 66% H₂ on perfusion. From day 5 after wounding until the final day of imaging, blood perfusion in the wound bed was significantly higher in the 66% H₂ group than in the other groups (P [66% H₂ vs. control] < 0.0001) (Fig. 1H, I), indicating better tissue survival and tube formation [56]. Furthermore, the oxygen saturation (SaO₂), total haemoglobin mass (tHb), and deoxyhaemoglobin (HHb) values were all higher starting at day 3 in the 66% H₂ group than in the 5% H₂ and control groups (Fig. 2I). The initiation of vessel formation by H₂ may happen earlier than day 5 post-wounding.

CD31 staining 11 days after wounding suggested the 66% H₂ group had the most pronounced tube formation (more than six times compared with that in the control group) (Fig. 1J, K). Whole-mounting scans targeting CD31 suggested that, from day 3 onward, 66% H₂ already induces visible vessel formation, especially in the proximal part of the wound site under the epidermis (Fig. 1L, M, Figure S2). In vitro tube formation test showed that the 66% H₂ group had a similar effect as the positive control group (bFGF) (Fig. 1N, O), and better than the 5% H₂ (with air), N₂ (no air), and 33% O₂ (No H₂) (Figure S3 A, B). Tube formation-related genes were upregulated in D1H but downregulated in D3H (Fig. 2P), indicating an early activation of tube formation by 66% H₂. Further whole-mount tissue scanning suggested H₂ accelerated the visible vessel formation of proximal wound since day 2 post-wounding (Figure S3A, B). These results are consistent with a role for H₂ in early vascularization, which could contribute to wound healing.

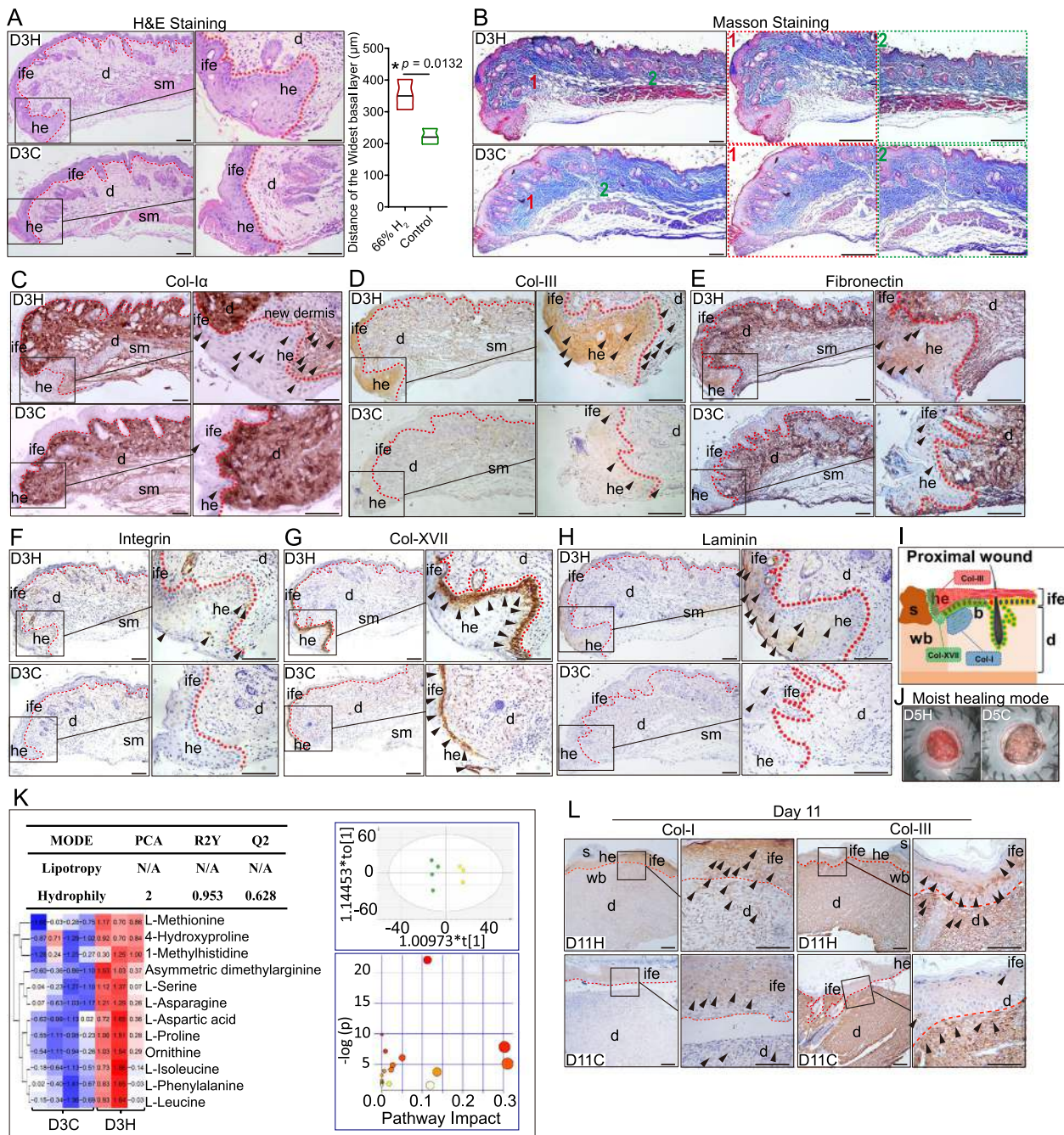


Fig. 2 H₂ treatment promoted different ECM components early deposit in the epidermis, dermis and dermis-epidermis-junction of proximal wound. **A** Representative H&E staining of the truncated region of epidermis at the wound edge at 3 days post-wounding between two groups; graph indicated the widest basal layer of hypertrophic epidermal wound edge. **B** Masson staining of different regions of wound edge at 3 days post-wounding between two groups. **C–H** IHC staining showing the expression of ECM components of Col-I, Col-III, Fibronectin, Integrin, Col-XVII, and Laminin, respectively in the wound edge between D3H and D3C groups. **I** Scheme of a proximal wound section indicating the histological localization of three kinds of collagens: Col-I (dermis), Col-III (epidermis), and Col-XVII (DEJ) expression after H₂ treatment during the re-epithelialization process. **J** Representative image of day 5 post-wounding indicating the moist healing mode possibly triggered by the early ECM deposition induced by H₂ treatment. **K** Overview of mapping of metabolic differences between the 66% H₂ and control groups as well as PCA analysis and pathway enrichment of differential metabolomes; R²_X = fraction of variance for the model; Q² = predictive ability of the model. **L** IHC staining showing the expression of Col-I and Col-III between D11H and D11C groups. Data in **A** processed unpaired *t* test, and were plotted as Mean ± SEM. **P* value < 0.05; ***P* value < 0.01; ****P* value < 0.001; no stars for *P* value > 0.05; scale bar = 100 μm. Red line indicates the boundary between the epithelium and dermis. Black arrowhead indicates positive-expressing cell. d, dermis; he, hypertrophic epidermal wound edge; ife, interfollicular epithelium; sm, smooth muscle

Hydrogen induced transcriptomic signatures associated with early ECM deposit, tube formation, cell migration and differentiation, and mitochondrial repair

Given the remarkable healing by 66% H₂ at day 3 after wounding (the epithelialization phase), we performed functional annotation and enrichment analysis of RNA-seq data from skin samples to identify underlying processes. Based on differences in expression between the 66% H₂ and control group (see the total DEGs in Table S4), 68 differentially expressed genes (DEGs) from D1H (day 1 H₂) vs D1C (day 1 control) (58/10, up/down) (Table S5), 18 DEGs from D2H vs D2C (12/6, up/down) (Table S6), and 24 DEGs from D3H vs D3C (18/6, up/down) (Table S7) were identified (adjusted *p* value ≤ 0.01 and |FC| ≥ 1.5), with no overlap between the sets of DEGs (Figure S4A–C). Heatmap cluster analysis of all DEGs identified 4 clusters (Figure S4D). Among the top-10 Gene Ontology Biological Processes (Figure S4E) in cluster I, the DEGs were mainly enriched in hormone response and signal transduction processes, which were upregulated mainly in D2H; genes in cluster II were enriched mostly in biological functions related to tube formation, cell migration and extracellular matrix (ECM) organization and were upregulated first in D1H, then gradually decreased to an equivalent expression level between D2H and D2C, and upregulated again in D3C; genes enriched in cluster III were mostly related to muscle cell differentiation and organization and were upregulated in the D3H group; and genes in cluster IV were involved in processes related to metabolism and were upregulated in D2C. Gene set enrichment analysis (GSEA) confirmed the pattern of DEG enrichment in ECM deposition-, cell adhesion-, and tube formation-related function in D1H (Figure S4F); muscle filament sliding and myofibril assembly related functions in D2H (Figure S4G); and myocyte migration and differentiation and mitochondria activity-related functions in D3H (Figure S4H).

Hydrogen induces early ECM deposition during the epithelialization process

Considering of the important role of ECM in epithelialization [12], the effect of 66% H₂ on early ECM deposition at 1–3 days after wounding was evaluated, which is when the proliferative phase normally starts and keratinocytes migrate into the wound bed. H&E staining showed a thicker epidermal layer on the hypertrophic epidermal wound edge in the D3H group as compared to the D3C group (*p* = 0.0132) (Fig. 2A). Furthermore, Masson staining revealed more dermal collagen deposition in the D3H group at both proximal and distal wounds (Fig. 2B). Consistently, immunohistochemical staining (IHC) showed that col-I (Fig. 2C) and col-III (Fig. 2D) were more highly

expressed in the D3H group, especially around the proximal area of the wound. Fibronectin (Fig. 2E), integrin (Fig. 2F), col-XVII (Fig. 2G), and laminin (Fig. 2H) were also elevated in the D3H proximal epidermis, indicating better DEJ formation after H₂ treatment. Scheme of the col-I, col-III, and col-XVII expression in the proximal wound edge was shown in Fig. 2I. ECM deposition may contribute to maintain the moist healing (Fig. 2J).

As additional evidence for the importance of the ECM, we examined the differential expression of metabolites. Twelve metabolites (Table S8, S9), all of which were amino acids, were differentially expressed on day 3 (Fig. 2K). Among them, L-proline, and especially 4-hydroxyproline, are known to provide raw materials for collagen synthesis [57]. Pathway categorization supported an increase in metabolites thought to contribute to an environment that supports ECM deposition in the wound bed after H₂ treatment (Table S10). Furthermore, correlation analysis of D3 non-target metabolism and RNA-seq showed similarly enriched genes in tight junctions and focal adhesion pathways (Figure S5).

We also examined ECM deposition at the wound site on day 2 by IHC, which demonstrated that col-I, fibronectin and laminin were more highly expressed in the D2H group than in the D2C group, at the proximal wound (Figure S6A–C), though no difference was observed in integrin expression (Figure S6D). This deposition of collagens in the 66% H₂ group lead all the way to day 11 post-wounding, especially for dermal Col-1 and epidermal Col-III (Fig. 2L).

Hydrogen induces α-SMA⁺/K14⁺ keratinocytes and α-SMA⁺ myofibroblast migration to the wound edge

Collagen and other ECM components can induce keratinocyte migration [58, 59]. To evaluate the effect of H₂ on epithelialization at the proximal wound edge (leading edge), we performed immunofluorescent staining of markers for myoepithelial cells/myofibroblasts (α-SMA), keratinocytes (K14), and IFE cells (K5). Day 3 whole-mount staining demonstrated more than 3 times the amount of α-SMA⁺/K14⁺ keratinocytes in the D3H group as compared to the control group (especially in the migration tongue region of hypertrophic epidermal leading edge) (Fig. 3A, B), indicating transformation from keratinocytes to a myoepithelial-like cell type. However, the IFE keratinocytes displayed slower proliferation rates in the D3H group than in the D3C group (Fig. 3C, D, *p* < 0.05), which may be due to a more advanced cell proliferation induced by H₂. Although not highly expressed, the epidermal keratinocytes at the leading edge produced more col-1 (α-SMA⁺/Col-1⁺) in the D3H group than in the D3C group (Fig. 3E, F). The transformation direction from keratinocytes to myoepithelial cells, were then

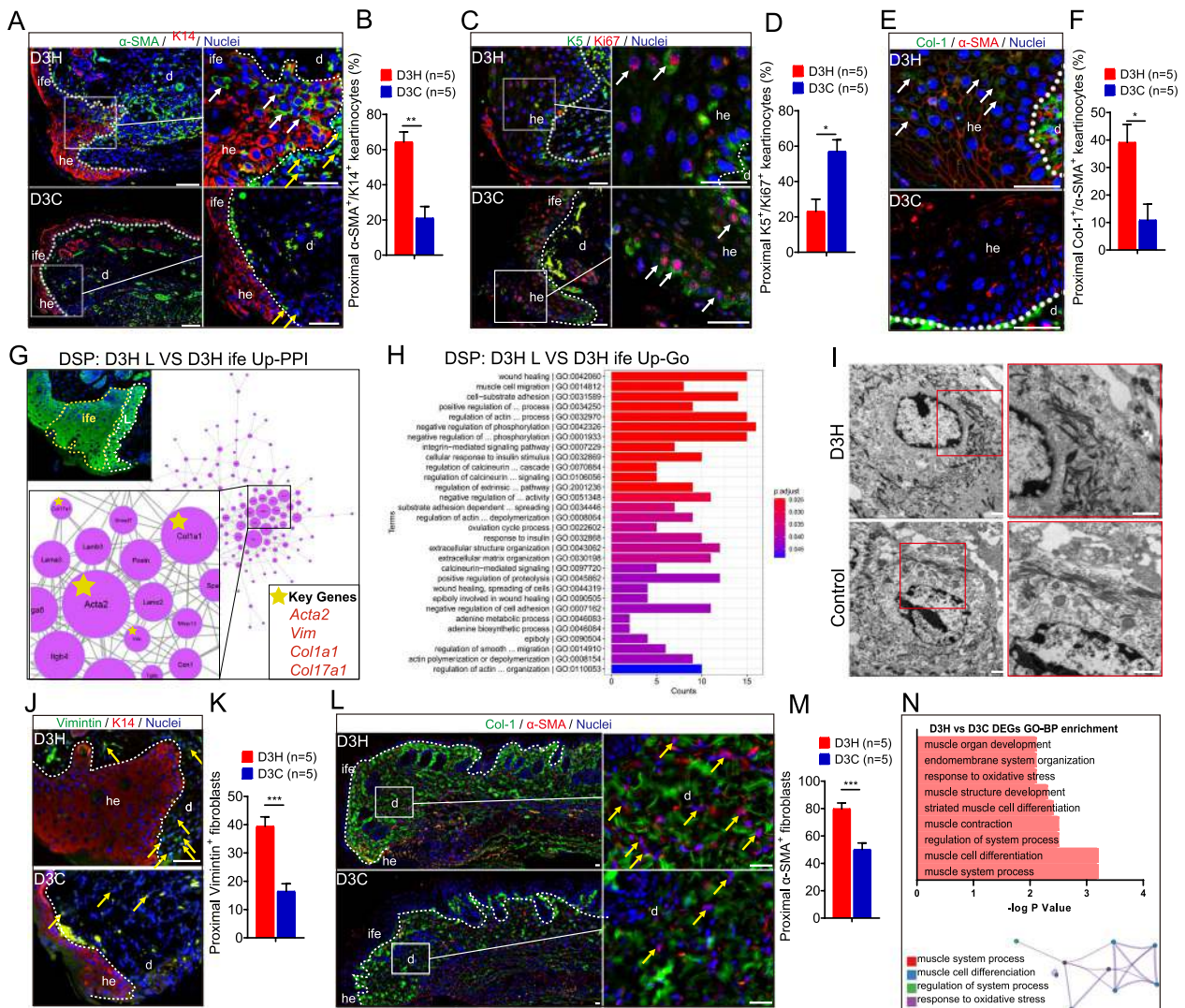


Fig. 3 H₂ induces myofibroblasts and fibroblasts migration and IFE towards α-SMA⁺ myoepithelial cell transformation in the proximal wound. **A, C, E, J** Detection of α-SMA/K14, K5/ki67, Col-1/α-SMA and Vimintin/K14 in the leading edge of the proximal wound at day 3 post-wounding. **L** Col-1/α-SMA co-expression in the dermal fibroblast of proximal wound at day 3 post-wounding. **B, D, F, K** and **M** quantification of double/single positive cells in **A, C, E, J** and **M**. **G, H** DSP transcriptome analysis of D3H proximal wound area (D3H leading edge vs D3H ife) showing the upregulated PPI network, key genes and up-GO biological processes in the keratinocytes of leading edge. White and yellow dotted circles indicate ROI of leading edge and ife, respectively. **I** Observation of keratinocyte tonofilament morphology in 66% H₂ and control groups by electron microscope. **N** GO-BP enrichment and enriched GO-BP clusters of D3H vs D3C DEGs by using metaspape online analysis. White dotted line indicates the boundary between the epithelium and dermis. White arrows in **A, C,** and **E** indicate co-positive IFE cells, yellow arrows indicate Vimintin⁺ (**J**) fibroblasts or Col-1⁺/α-SMA⁺ co-positive myofibroblasts (**L**). Data in **B, D, F, K,** and **M** processed Unpaired T test, and were plotted as Mean ± SEM. *P value < 0.05; **P value < 0.01; ***P value < 0.001; no stars for P value > 0.05; Scale bar in **A, C, E, J,** and **L** = 100 μm; Scale bar in **I** = 1 μm. d, dermis; he, hypertrophic epidermal wound edge; ife, interfollicular epithelium. DSP, digital spatial profiler

proved by digital spatial profiler transcriptome analysis (D3H Leading edge vs D3H ife of the proximal wound). Seeing from Fig. 3G, key genes selected after up-PPI analysis include Acta2 (α-SMA), Vim (Vimintin), Col1a1 (col-I), and Col17a1 (col-XVII). D3H L up-GO BP were mostly enriched in myoepithelial cell-related functions (Fig. 3H). Electron microscopy demonstrated a higher

density of tonofilaments arranged around the plasma membrane of keratinocytes at the leading edge of the D3H group (Fig. 4I); the correlation analysis of transcriptomics and metabolomics also revealed that, the focal adhesion-related function was enriched in D3H group (Figure S5). These results could support better migration ability for myoepithelial-transformed keratinocytes [60].

Furthermore, both α -Vimentin⁺ fibroblasts (Fig. 3J, K, $p < 0.001$) and α -SMA⁺ myofibroblasts (Fig. 3L, M, $p < 0.001$), which are two of the main sources of collagen, were more abundant in the proximal wound of the D3H group. In vitro IF staining also proved that fibroblasts (HPF, (Figure S7E)) and keratinocytes (HaCat, Figure S7B) were producing more col-1 after H₂ treatment. Besides, the primary cell HUCP-MSCs have been identified to maintain the MSCs phenotypes (Figure S7A, B). H₂ promoted the HUCP-MSCs transformation into a myofibroblast phenotype (Vemintin⁺, α -SMA⁺) (Supplemental Figure S7C) with better collagens producing (Supplemental Figure S7C) abilities. Consistent with all the staining results, transcriptome analysis of D3 identified top Gene Ontology biological process (GO-BP) enrichment categories involved muscle cell development, differentiation, and contraction (Fig. 3N).

Hydrogen induces early IFE and HF stem cells proliferation

IFE stem cells (IFESCs) are thought to promote wound healing and replace irreversibly lost skin [61], while hair follicle stem cells (HFSCs) around the wound replenish the basal layer and reconstitute non-proliferative, transcriptionally active spinous and granular layers [17, 62]. To characterize the early proliferation and distribution of IFESCs and HFSCs in early wounding, we performed whole mount tissue scans. More $k14^+/Ki67^+$ basal IFESCs were identified in the D1H (Fig. 4A, D) and D2H groups (Fig. 4B, E), particularly at the leading edge (L, 0–1 mm from the wound site). Furthermore, the proportion of $k14^+/Ki67^+$ HFs was more abundant in the D1H group in the L, M (middle), and D (distal) edges of the wound site (Fig. 4D). However, 3 days after wounding, there were fewer $k14^+/Ki67^+$ basal cells and HFs in the D3H group, especially in the L and M parts of the wound (Fig. 4C, F), indicating an advanced activation for the IFESCs proliferation triggered by H₂.

We further characterized IFESCs and HFSCs by examining the expression of specific markers in proliferating cells after H₂ treatment. The results demonstrate that $p63^+/Ki67^+$ basal IFE cells were more abundant in the D1H and D2H groups in the L, M, and D parts of the proximal wound after H₂ treatment (Fig. 4G, J).

Additionally, there were more $k15^+/Ki67^+$ hair follicles in the D1H group and $k15^+/Ki67^+$ basal IFE cells in the M and D wound in the D2H group (Fig. 4H, K). There were also more $Lgr6^+/Ki67^+$ basal IFE cells in the D1H and D2H groups in the L, M, and D parts of the wound site (Fig. 4I, L), while $Lgr6^+/Ki67^+$ HFs were more abundant in the M and D parts in the D1H and D2H groups (Fig. 4I, L). All $p63^+/Ki67^+$, $k15^+/Ki67^+$, and $Lgr6^+/Ki67^+$ basal IFE cells and HFs were decreased for the first 3 days after H₂ treatment (Fig. 6J–L). Thus, H₂ treatment induces early proliferation of basal IFE stem cells and HFSCs that contribute to epidermal thickening and wound closure.

Hydrogen alleviates inflammatory responses by reducing especially the Th₁ and Th₁₇ population during aseptic wound healing

Inflammation also influences wound healing and matrix deposition [63, 64]. Therefore, we sought to determine the effect of 66% H₂ treatment on Th cell subsets. Flow cytometry of mouse spleens 24 h after wounding showed the CD4⁺ and CD8⁺ T cells had no significant differences among the three groups (Figure S8A), while the population of Th₁ and Th₁₇ subgroups were reduced by H₂ treatment (Figure S8B, D). No significant differences were observed in the other two subsets of Th₂ and Treg cells (Figure S8C, E). A representative gating strategy was shown in Figure S8F. The splenic FCM detection revealed H₂ alleviated Th₁- and Th₁₇-related systemic inflammation during the early stage of wound healing. Due to the aseptic wound (daily oral intake enrofloxacin for each group) [65], tissue cytokine profile for the H₂ group has no big difference with the control and NAC group, though TNF- α , IL-1 β were reduced and IL-10 was slightly increased 24 h after wounding in the 66% H₂ group (Figure S8G).

H₂ promoted keratinocytes in re-epithelialization and fibroblasts/MSCs in migration possibly due to maintaining the mitochondrial functions

In the re-epithelialization phase of wound healing, epithelial cells migrate to the wound site, cover the granulation tissue, and then converge in the middle. In vitro live cell imaging revealed an enlarged HaCat cell colony area in the

(See figure on next page.)

Fig. 4 H₂ treatment promoted in vivo early epidermal stem cells proliferation at days 1–3 after wounding. **A–C** Panoramic scanning of wound edge and the representative immunofluorescence images of K14 (green) and ki67 (red) expression in the leading edge (L, 0–1 mm from wound edge), mid-end (M, 1–2 mm from wound edge) and distal end (D, 2–3 mm from wound edge) of the wound; **D–F** Statistics of $K14^+/ki67^+$ basal cells and hair follicles in the immunofluorescence. **G–I**. Representative immunofluorescence of p63 (green) and ki67 (red), K15 (green) and ki67 (red), and Lgr6 (green) and ki67 (red) on skin section showing their expression in the leading edge (L), mid-end (M) and distal (D) of the proximal wound in epidermal and hair follicle cells from 1 to 3 days after wound. **J–L**. Statistics of $p63^+/ki67^+$, $K15^+/ki67^+$, and $Lgr6^+/ki67^+$ basal cells and hair follicles in the immunofluorescence from 1 to 3 days after wounding. White arrow indicates co-positive basal cell; yellow arrow indicates co-positive follicle cell. Data in **D–F**, **J–L** processed two-way ANOVA test, and were plotted as Mean \pm SEM. * P value < 0.05; ** P value < 0.01; *** P value < 0.001; no stars for P value > 0.05; Scale bar = 100 μ m

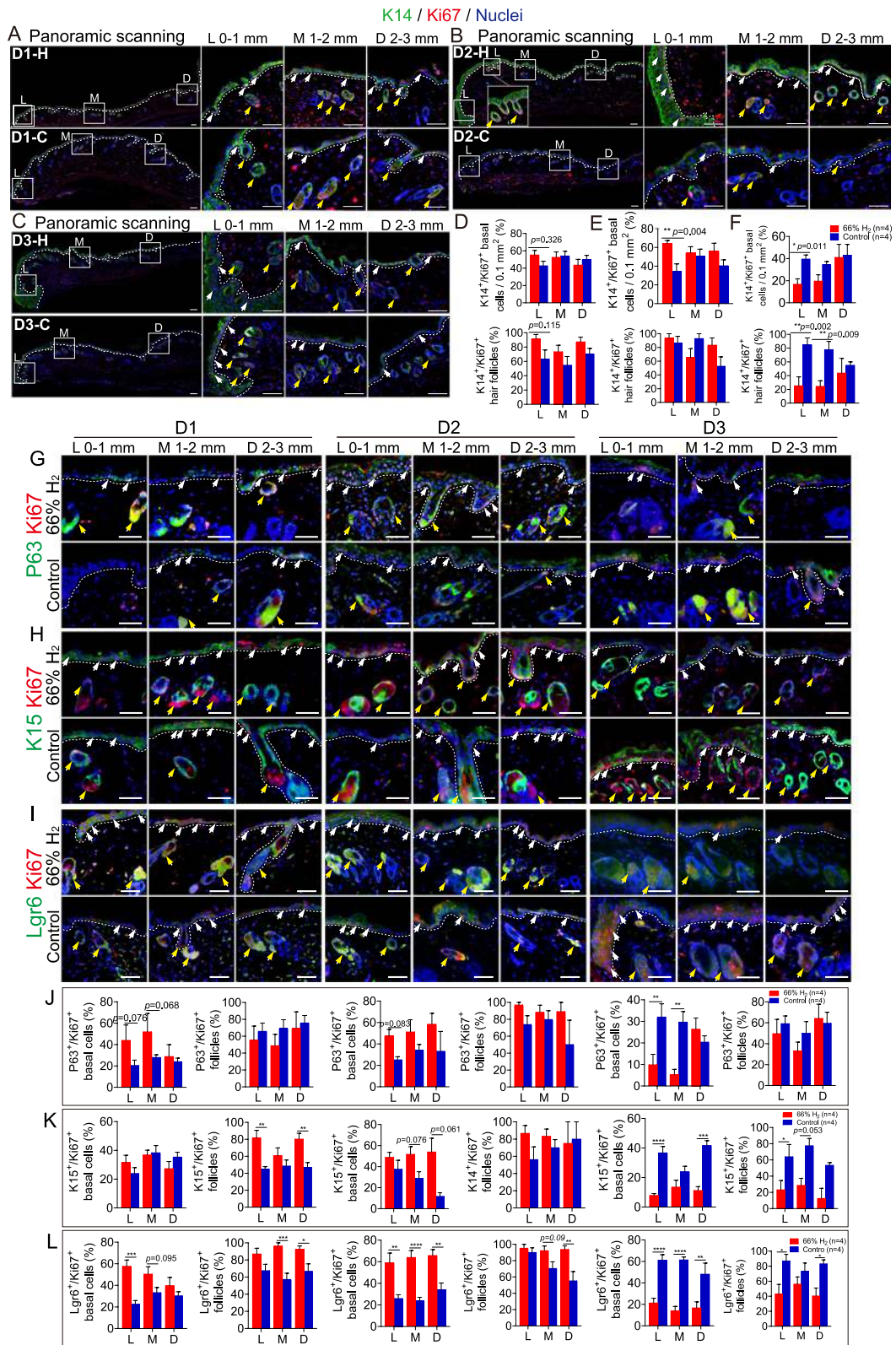


Fig. 4 (See legend on previous page.)

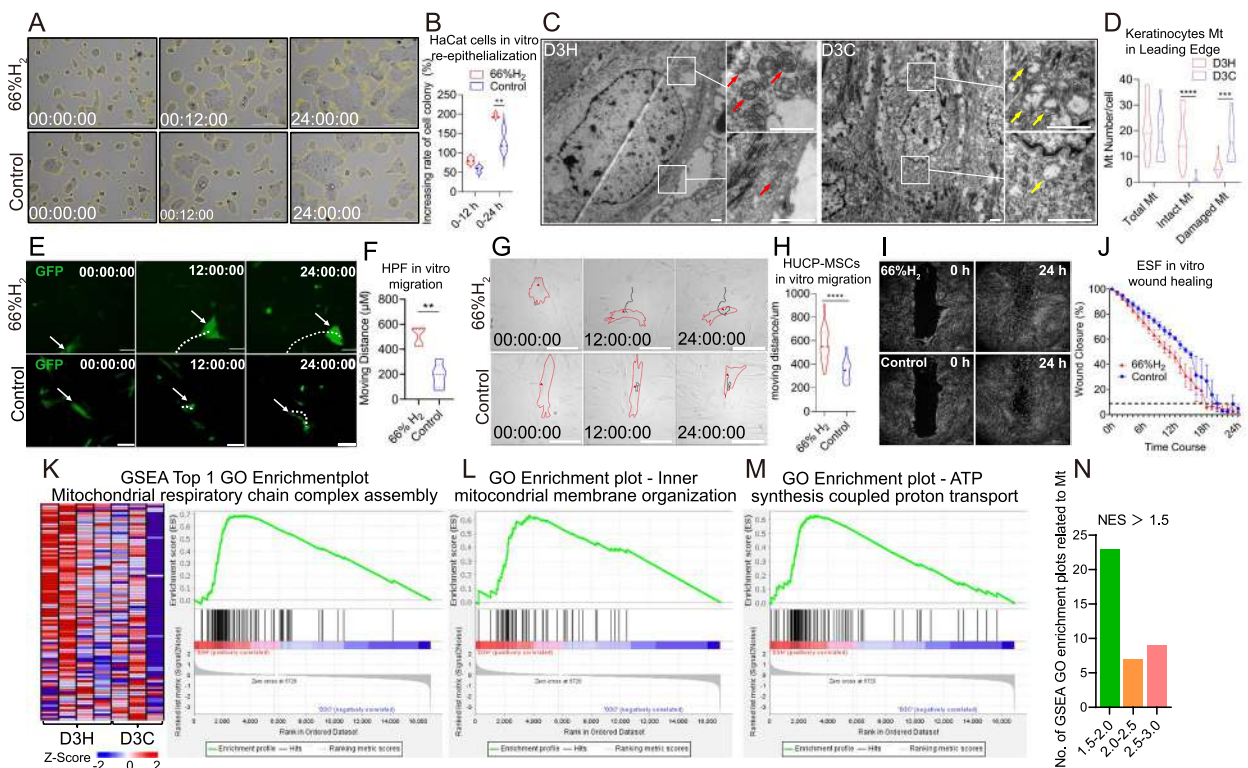


Fig. 5 H₂ promoted *in vivo* and *in vitro* keratinocytes and fibroblasts cells viability by accelerating the re-epithelialization, migration and mitochondrial functions. **A**. Representative images of HaCat cell epithelialization. Images were captured every two hours using a live cell imaging system, and the 0, 12 and 24 hour images were presented. **B**. The increased rate of the total colony area in 12 and 24 hours. **C**. Comparison of mitochondrial morphology 3 days post-wound for the D3H and D3C groups observed by electron microscope. The right two images in each panel are enlargements of the white frames in the left images. Red arrows indicate intact mitochondria, while yellow arrows indicate damaged mitochondria. **D**. Comparison of total mitochondria, intact mitochondria and damaged mitochondria numbers between D3H and D3C groups. **E** and **G**. Representative images of HUCP-MSCs and HPF fibroblasts migration at 0-h, 12-h, and 24-h time points in H₂ medium and control groups. **F**, **H** Graphic analysis of HUCP-MSCs and HPF fibroblasts total moving distance in 24 h. **I**. Cell migration ability examined by wound-healing assay in H₂ medium and control groups. **J** Wound-healing curve analysis under different conditions. **K** Heatmap and enrichment plot showing genes related to mitochondrial respiratory chain complex assembly, which is the top 1 GO enrichment function in D3H. **L**, **M** Top GO enrichment plots in D3H related to inner mitochondrial membrane organization and ATP synthesis-coupled proton transport, which indicates more intact and functional mitochondria in D3H. **N** GSEA GO enrichment plots enriched in Mt related functions for D3H (NES > 1.5). White and black dotted lines in **E** and **G** indicate the migration route of fibroblasts. Red dotted line in **G** outlines the representative HUCP-MSCs. Data in **B** and **D** processed two-way ANOVA test, and data in **F**, **H**, and **J** processed unpaired *t* test. Data were plotted as mean ± SEM. **P* value < 0.05; ***P* value < 0.01; ****P* value < 0.001; no stars for *P* value > 0.05; Scale bar in **A** and **G** = 200 µm, scale bar in **C** = 2 µm, scale bar in **E** = 100 µm, scale bar in **I** = 1000 µm

H₂ group (Fig. 5A, B). Furthermore, we performed electron microscopy 3 days after wounding and observed the Mt of the keratinocytes in the leading edge (0–1 mm from wound edge). The D3H group showed increased total Mt numbers, with more intact and fewer damaged Mt (Fig. 5C, D).

To confirm the cell migration ability enhanced by H₂, HPF fibroblasts and HUCP-MSCs were plated and observed by live cell imaging system for 24 h after H₂ medium treatment. For the HPF cells, the total moving distance in the H₂ group was 2.5 times higher (*p* < 0.01) than that in the control group (Fig. 5E, F; videos provided in supplemental movies 1 and 2). Similarly, at 24 h, the total moving distance of HUCP-MSCs

were significantly higher in the H₂ group than in the control group (*p* < 0.0001) (Fig. 5G, H). In a live cell scratch assay, human embryonic skin fibroblast ESF cells healed faster in the H₂ group than in the control group (Fig. 5I, J).

The GSEA from D3H vs D3C up-Go genes were enriched in mitochondria (Mt) structure and function (Figure S4H), which are important for cell migration. Detailed GO-plots related to Mt organization and energy generation were extracted for the D3H up-GO GSEA (Fig. 5K–N). All these mitochondrial functions promoted by H₂ give promise to a better cell viability for keratinocytes, fibroblasts, and MSCs in the wound edge.

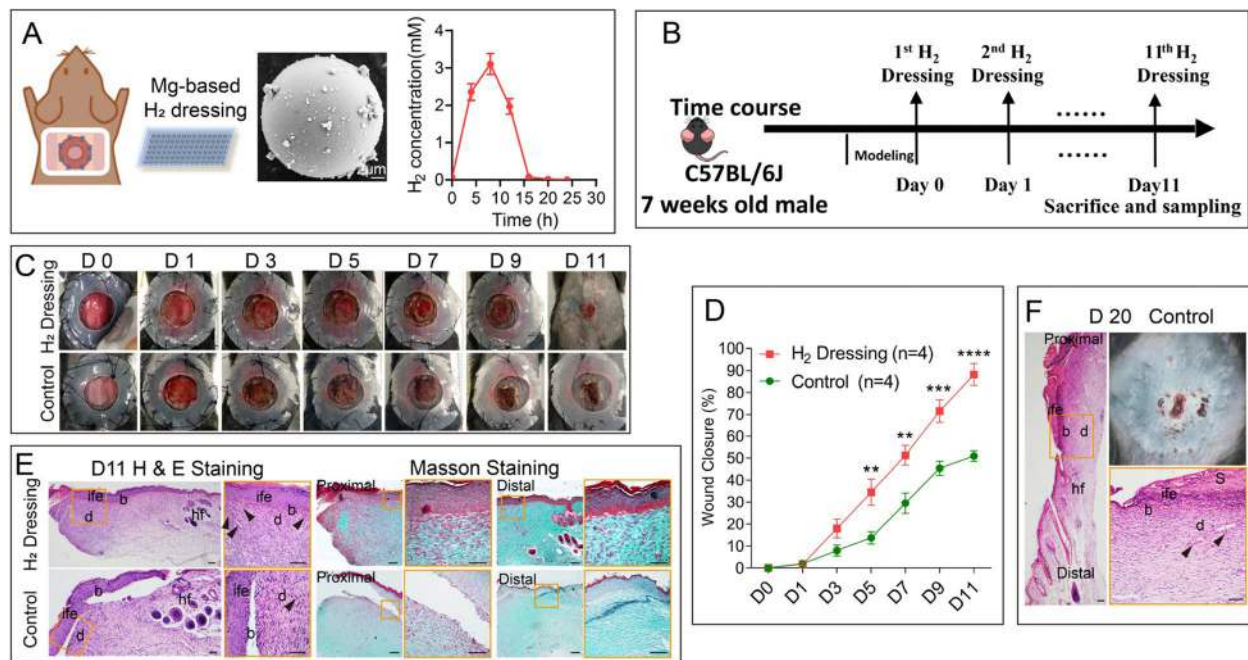


Fig. 6 Daily topical treatment of H₂ dressing significantly promoted cutaneous wound healing. **A** Left: scheme images of Mg-based H₂ dressing in cutaneous wound healing treatment; Middle: scanning electron microscope (SEM) image of Mg microparticles; right: H₂ release curves of Mg-based dressing. **B** Timeline of animal experiments and daily H₂ dressing treatment (or normal dressing condition). **C** Representative wound area images captured every 2 days after modeling. **D** Comparison of wound closure percentage after modeling between H₂ dressing and control groups. **E, F** H&E staining and Masson staining showing the tissue remodeling 11 days and 20 days post-wounding. Data in **D** was analyzed by two-way ANOVA test. All of the data are plotted as mean ± SEM. **P* value < 0.05; ***P* value < 0.01; ****P* value < 0.001; *****P* value < 0.0001; no stars for *P* value > 0.05; scale bar in **A** = 2 μm, scale bar in **E** = 100 μm. Red dotted line in **E** (H&E staining) indicates the boundary between the epithelium and dermis. Black arrowheads in **E** and **F** indicate blood capillaries in the dermal layer of the wound. b, basal layer; d, dermis; hf, hair follicles; ife, interfollicular epithelium; s, scab

H₂ promote the early repair of muscle and skin nerve injuries

Since hydrogen can promote early epithelization and tissue remodelling during wound healing processes, it is also likely to have a good repair effect on other tissue injuries such as muscle and nerve. In the muscle contusion model (Figure S9A), the swelling and blood perfusion of gastrocnemius muscle was significantly relieved in the 66% H₂ group since day 2 onward (Figure S9B-D). These results indicated early repair functions of H₂ in soft tissue muscle damage. On the other hand, NFH (neurofilament, heavy polypeptide) was used as a marker to reveal the possible function of hydrogen in nerve injury repair and axons maturation. More NFH⁺ cells were observed in the 66% H₂ group of proximal wound edge on day 3 and day 12 post-wounding, suggesting the cutaneous nerve was repaired by H₂ treatment at an early stage. Other kinds and more complicated tissue injury restoration will be further explored in our future research.

Topical treatment of H₂-releasing dressing promoted wound healing

Considering the application in human wound care, topical H₂-releasing dressing could be a candidate strategy which is more convenient and easier to perform. As it is

shown in Fig. 6A (left), Mg-based H₂-releasing dressing is prepared and topical treated on top of the wound. The Mg balls are all microparticles with the average diameter of 20 μm (Fig. 6A, middle). The H₂ release lasted for more than 12 h (Fig. 6A, right). H₂ dressing group healed faster than the control group (Fig. 6C, D), with more blood capillaries formation and collagen deposition on day 11 post-wounding (Fig. 6E). The day 20 HE staining in the control group (Fig. 6F) suggested that, even though given doubled time the wound closure in the control group reached a same level as the H₂ group on day 11 post-wounding, the healing effects might be not as good as the H₂ group, because of the incomplete epithelial layer, unclear basal layer boundary, and less capillaries formation. Additional research into longer-lasting and more thorough healing benefits for hydrogen dressing is still needed, such as in scar formation and tissue remodeling.

Discussion

Evaluation of the H₂ induced novel wound healing pattern
The speed and effect of re-epithelialization during wound healing is largely attributable to ECM [12] and EpSCs [11]. Therefore, it is vital and uplifting to

find new strategies that induce autologous ECM accumulation and EpSCs activation for wound healing. In addition to these two factors above, “TIME” is usually being applied in the evaluation of healing effect. Our current study discovered that molecular hydrogen induced a new healing pattern, particularly characterized by fast re-epithelialization, early ECM deposition and EpSCs activation. For the evaluation of the “TIME” indicators, H₂ promoted the effect of wound healing in a comprehensive way. “T” for tissue remodeling is improved by good DEJ, massive blood vessel formation and dermal collagens deposition. In the “I” of inflammation, we proved that H₂ reduced the splenic Th₁ and Th₁₇ Th-cells subgroup distribution. This shift of Th-cells subgroup is reported to be important in facilitating wound healing [66]. For “M” of moisture balance, we revealed that H₂ induced a natural moist-like healing mode, with less blood clots formation. “E” is representing of edge of wound, and H₂ greatly promoted the re-epithelialization progress, with fast keratinocytes migration and early EpSCs proliferation in the leading edge. However, it has to be further investigated, if our perspective can be applied to all wounds. The animal model of sterile wound model can be one of the limitations in our study. Although there are evidences showing the positive role of hydrogen in multiple wound care, the therapeutic impact and our concept in the mechanism of hydrogen in the treatment of complicated wounds, still need to be further established. Because wounds such as in diabetic wounds and burns, are frequent in clinical practice.

Early deposition of ECM components promoted by H₂ and contributed to fast re-epithelialization, tight DEJ and natural moist healing environment

As the most abundant protein in the ECM [67], collagen (especially type I and type III collagen) synthesis, deposition, and release are favourable for EpSCs activities in the skin. In our study, we observed early ECM deposition (1–3 days after wounding) especially for collagens after H₂ treatment (Fig. 2C–H). This was confirmed by RNA-seq (Figure S3E, F) and untargeted metabolome analysis (Fig. 2K). Though in some hard-to-heal wound studies, H₂ was proved to promote collagen synthesis by masson staining [40] and IHC staining for Col-1 [42], our study is the first comprehensive and histological reveal of H₂-induced early deposition of massive ECM components during re-epithelialization of wound healing. In order to reform the basement membrane beneath the epidermal basal layer, both keratinocytes and fibroblasts will contribute to ECM components synthesizing [12]. Early

dermal col-I and especially epidermal col-III in the proximal wound were found accumulated in the H₂ group, which indicated better structural integrity of the ECM and refined tissue functions [68]. This is possibly related with the transformation from keratinocytes to myoepithelial-like cells (K14⁺/αSMA⁺, Fig. 3A, G). In skin tissue, the ratio of col-I/col-III normally increased with time from foetus to adult [69, 70]. The cross-linking pattern of collagen is always important to determine the scar-free wound [69–72]: foetal skin tissue deposit more col-III than adult skin, which contributes to scar-less wound healing; on the contrary, fibrillar col-I is dominant in adult skin, leading to scar formation. During wound healing, col-I/col-III ratio stayed dynamically, first decreased and then increased to normal level [72]. Therefore, the massive deposition of col-III in the proximal wound (Fig. 2D) after H₂ treatment may indicate a youthful state of skin, leading to faster re-epithelialisation. In addition to col-I and col-III, H₂ induced early fibronectin deposition would also provide a scaffolding for epithelial migration [73], which is similar to fetal scarless wound healing pattern [74]. Skin basal keratinocytes separate the epidermis and dermis, and maintain the two layers attached together. This function is dependent on DEJ-related proteins, of which Laminins [75] and col-XVII [76] are two of the most important members. The higher expression level of laminin (Fig. 2H) and especially col-XVII (Fig. 2G) in the proximal epidermal keratinocytes indicated better DEJ induced by H₂. Provision and maintenance of a moist condition (Fig. 2J) is favourable for establishing an ideal microenvironment for healing processes. Collagen dressing is therefore always chosen as one of the wound care strategies [77, 78]. Instead of topical application of collagens, early autologous collagens accumulation in the proximal dermal and epidermal wound was found induced by H₂ and persisted in the whole healing processes. Untargeted metabolome analysis for the wound bed tissue revealed that most of the identified differential metabolites in H₂ group (Fig. 2K) are related with the components, precursors, or inducers of collagen synthesis, such as 4-hydroxyproline [79], L-proline [80], and asymmetric dimethylarginine [81]. Taken together, ECM deposition promoted by H₂ could contribute to the fast re-epithelialization, tight DEJ, and natural moist healing environment.

The early activation of autologous EpSCs proliferation and differentiation regulated by H₂ treatment

Once the cells at the wound edge begin to migrate, epithelial cells behind the edge proliferate; this continues until new epithelium covers the damaged tissue

[82]. Epidermal growth and thickening rely on the surrounding components such as the ECM, as well as on the activation of EpSCs. To restore the functional epidermal barrier, EpSCs proliferation is followed by differentiation [83, 84]. When IFESCs and HFSCs are recruited to the IFE after injury, they progressively lose their initial identities and differentiate [85]. Different stem cell markers involved in IFESC and HFSCs niches [86], such as K5 [87], Lgr6 [88], K15 [89], and p63 [90] were examined here. We observed early proliferation (since day 1 post-wounding, about 1–2 days earlier than the control group) of IFESCs and HFSCs during the first 3 days post-wounding (Fig. 4A, B, G–I), as well as thickening of proximal stratum corneum in the H₂ group (Fig. 2A), though the differentiation trajectory of these stem cells still needs to be tracked. Two other stem cell-related studies reported that H₂ prolonged the replicative lifespan of bone marrow multipotential stromal cells in vitro [46], and protected hematopoietic stem cell from irradiation injury [47]. In vivo studies on the effect of hydrogen on stem cell proliferation and differentiation, and the relationship between hydrogen and EpSCs in wound healing have not been studied. Our study revealed that H₂ promoted the early EpSCs proliferation and differentiation in different time series (day 1–3) and space series (leading edge, mid-end and distal part of wound) during wound healing for the first time. The following differentiation of the EpSCs then surprisingly turned out to be K14⁺/α-SMA⁺ myoepithelial-like cells, which may further contribute to collagen deposition, epidermis migration and the maintenance of the youthful state of cells. In addition, some studies have already mentioned the mobilization and contribution of MSCs/stroma cells to regeneration of injured epithelia [91]. In our study, in vitro experiment also proved that H₂ could activate MSCs and induce the transformation from MSCs towards myofibroblast-like direction, with the phenotypes of αSMA⁺, Vimentin⁺, and better ability of collagen producing (Figure S7) and moving (Fig. 5G, H), which could further contribute to the wound closure. The combined major benefits of earlier ECM deposition and stem cell proliferation and differentiation after H₂ treatment, as well as vessel formation and cell migration, promoted haemostasis, re-epithelialization, and reduced scab formation. However, whether EpSCs in a collagen-rich environment are more likely to differentiate to keratinocytes remains unclear [92]. Besides, in order to identify which EpSCs subgroups were first triggered by H₂ and their subsequent differentiation trajectory throughout wound healing, more studies on the EpSCs lineage tracking are still needed.

Potential mechanism of H₂-induced high cellular activity in various cells

Notably, though most of the current reports have focused on H₂'s anti-ROS and anti-oxidative functions [93], our study revealed that these anti-oxidative functions are not the key means by which H₂ (O₂-independent) accelerates wound healing. One direct evidence could be NAC, which is well-known as an effective ROS scavenger [94], had no statistical effect on the healing processes in our study (Fig. 1C, D). Meanwhile, the healing effects in 33% O₂ treatment had no significant difference comparing with the control group (Fig. 1C, D). Consequently, the mechanism of selective antioxidant cannot explain the H₂ induced early accumulation of ECM and activation of EpSCs observed in our study, and that, these H₂-induced beneficial effects in wound healing is not O₂ dependent. Besides, we discovered that H₂ promoted cell viability in vitro of different cell types, which manifested in more tube formation for endothelial cells (Fig. 1N), faster cell migration for fibroblasts (Fig. 5E, G, I), and better epithelialization for keratinocytes (Fig. 5A). This is also reflected in EpSCs early proliferation, however, the proliferation seemed to be under a strict regulation, with proliferation during the first 2 days post-wounding (Fig. 4A, B, G–I) and differentiation from day 3 onward (Fig. 3A, G). The promoted cell viability was quite consistent with what we observed in the H₂ group in vivo, including early blood vessel formation (visible since day 3 post-wounding, Fig. 1L, M), fibroblast aggregation (approximately day 3 post-wounding, Fig. 3J, L) in the proximal wound and faster re-epithelialization (visible since day 3 post-wounding, Fig. 2A). These observations above revealed that H₂ was able to boost the cell viabilities of diverse cells in different ways, at different time points but in the same histological space during wound healing. Combining with our results (Fig. 5C, D, K–N; Figure S3H), one of the possible explanations for the better cell viability could be H₂ induce robust mitochondrial activities and less structurally aberrant mitochondria during wound healing. This will further promote such as cell proliferation [95] and migration [96] abilities. Though the mechanism of H₂ remains unclear, recent studies revealed that H₂ may be multi-targeted and mainly based on enzymatic reactions. Higher organisms may have hydrogen metabolism abilities based on hydrogenase, especially for the mitochondrial-related hydrogen metabolism [97, 98]. The cell membrane may have the enzyme activity of hydrogen metabolism, and ion channels are also possibly regulated by H₂ [99, 100]. Recent study also put forward that, Fe-porphyrin is a

H₂-targeted molecule, acting as a biosensor and catalyst for H₂ [101, 102]. Taken together, our study indicates that the role of H₂ may function at the level of very basic biological processes of life, which needs to be further explored in the future.

Conclusion

For this study, we used a H₂ chamber (no requirement for body fixation or anaesthesia) with a murine aseptic wound model. Considering its both inhalation and wound surface contact with H₂, we also put efforts in the nasal inhalation (chronic wound) [103] and topical H₂ sustained-release dressings (cutaneous wound) (Fig. 6) treatment in wound care, and both non-invasive interventions received good effects. Clinical investigations and other wound models with more

complexity are also being conducted. There is also evidences that topical hydrogen intervention improved the wound healing in vivo [104]; however, comparing to focusing on the anti-infection and anti-inflammation effects, our research, instead, have indicated more functions of H₂ in wound healing. Without combination with any specific medicine, we revealed that H₂ alone was able to increase the rate of wound healing, with advantages (Fig. 7) including but not limited to promoting ECM deposition, autonomous stem cell early proliferation, blood vessel formation, cell viability, and natural moist healing pattern. We believe that this highly effective therapeutic method of H₂ treatment holds promise for further clinical wound treatment, as well as applications in the tissue damage repair, regeneration and other wider fields.

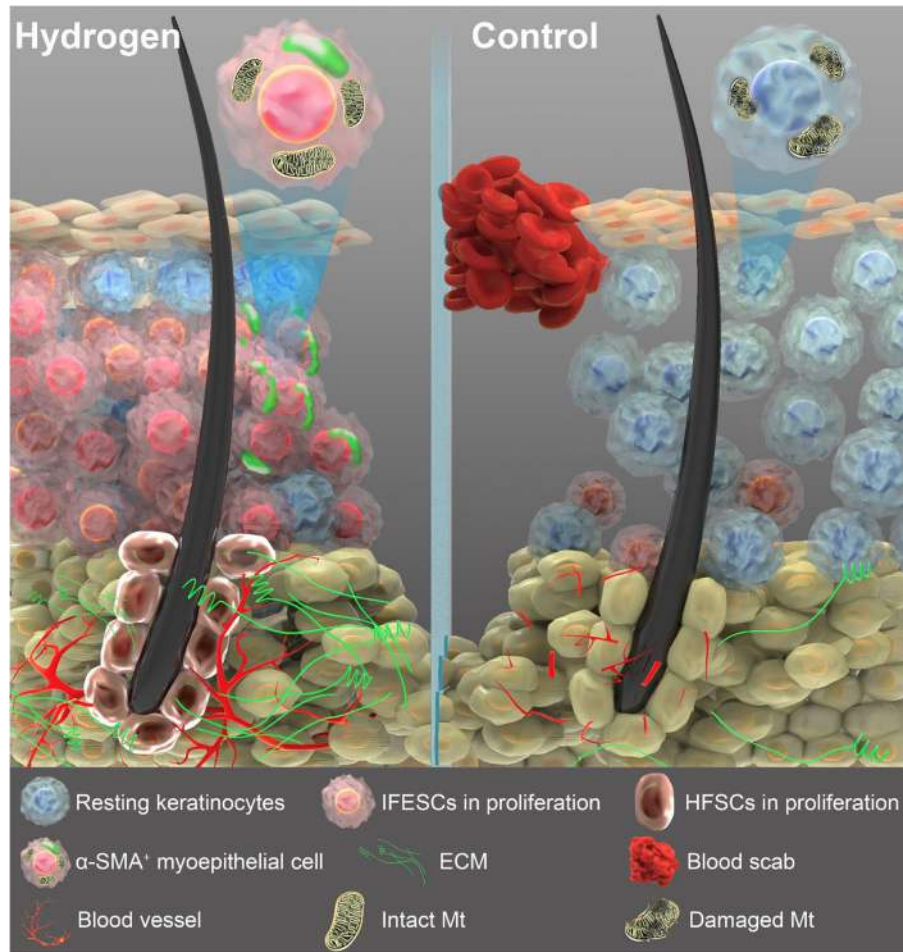


Fig. 7 Schematic representation of the skin under H₂ treatment and normal conditions during the early stage wound healing. In addition to anti-inflammation (especially for Th1- and Th17-related systemic inflammation), H₂ treatment brings multiple other benefits (shown in the figure) including faster epidermis thickening, earlier proliferation (red nuclei) of epidermal stem cells (basal cells and hair follicle cells), early differentiation of basal cells in the wound edge (differentiate towards α-SMA⁺ cell type), earlier and better ECM deposit, faster blood vessel formation, mitochondrial damage repair, and moist healing process (less blood scab formation)

Abbreviations

DEJ	Dermal and epidermal junction
DEGs	Differentially expressed genes
DSP	Digital spatial profiler
ECM	Extracellular matrix
EpSCs	Epidermal stem cells
GO-BP	Gene Ontology biological process
GSEA	Gene set enrichment analysis
HF _s	Hair follicles
H&E	Hematoxylin and eosin
HUCP-MSCs	Human umbilical cord primary mesenchymal stem cells
IFE	Interfollicular epidermis
IHC	Immunohistochemical staining
Mt	Mitochondria
NAC	N-acetyl-L-cysteine
ROS	Reactive oxygen species

Supplementary Information

The online version contains supplementary material available at <https://doi.org/10.1186/s41232-023-00271-9>.

Additional file 1: Supplemental Figure S1. H₂ slightly increases growth factors concentration at wound sites at day 1-3 after wounding. **A, B.** Profiles of tissue growth factors PDGF and EGF among the three groups at time points of day 1, day 2 and day 3 post-wounding. **C, D.** Concentrations of tissue growth factors bFGF and TGFβ-1 among all three groups at day 3. Data in **A** and **B** processed Two-way ANOVA test, and data in **C** and **D** processed unpaired t test. All data were plotted as Mean±SEM. * *P*-value < 0.05; ** *P*-value < 0.01; *** *P*-value < 0.001; no stars for *P*-value > 0.05.

Supplemental Figure S2. Whole-mount scanning showing H₂ promoted early tube formation at the first 2 days after wounding. **A** and **B.** Panoramic scanning of wound edge and the representative immunofluorescence images of CD31 (green) and k14 (red) expression in the leading edge (L, 0-1 mm from wound edge), mid-end (M, 1-2 mm from wound edge) and distal (D, 2-3 mm from wound edge) of the wound at day 1 and day 2 post wounding respectively. White dotted line indicates the boundary between the epithelium and dermis. White arrowhead indicates tube formation. Scale bar = 100 μm. **Supplemental Figure S3.** Whole-mount scanning showing H₂ promoted early tube formation at the first 2 days after wounding. **A** and **B.** Representative microscopic images and the quantification of *in vitro* blood vessel formation of Human Umbilical Vein Endothelial Cells (HUVEC) at 12 h after different treatments. Red hatched line outlines the newly formed tubes. Data in **B** were processed unpaired multiple T test. All of the data are plotted as Mean±SEM. * *P*-value < 0.05; ** *P*-value < 0.01; *** *P*-value < 0.001; no stars for *P*-value > 0.05. Scale bar = 100 μm. **Supplemental Figure S4.** Comprehensive gene set function enrichment analysis of differential gene expression induced by 66% H₂ treatment at the first 3 days post wounding. **A.** Heat map showing the differentially expressed genes (DEGs) among the three time points (D1H vs D1C, D2H vs D2C, D3H vs D3C). **B.** Venn diagrams showing the overlapping number of DEGs among the comparative data of three time points. **C.** Counting of total, up- and downregulated DEGs among the comparative data of three time points. **D.** Heat map showing four clusters identified from all the DEGs. **E.** GO-BP analysis in each individual cluster, the GO terms for genes related with extracellular matrix organization and muscle cell differentiation were significantly enriched in D1H and D3H, separately. **F.** Top 10 enriched up and down GO-BP in D1H by GSEA. **G.** Top 10 enriched up and down GO-BP in D2H by GSEA. **H.** Top 10 enriched up and down GO-BP in D1H by GSEA. **Supplemental Figure S5.** Transcriptomics and metabolomics correlation analysis reveal that differential genes and metabolites of the D3H group are enriched in tight junction and focal adhesion pathways. **A.** Correlation plot of DEGs and differential metabolites between D3H and D3C. **B.** Count of D3H vs D3C DEGs enriched in KEGG pathways. **Supplemental Figure S6.** ECM components col-I, fibronectin, laminin, and integrin deposition 2 days after wounding are increased in the H₂ group especially in the proximal wound edge. **IHC** staining showing the difference between D2H and D2C in ECM deposit of day 2 post wounding. **A-D** indicated Col-1, fibronectin,

laminin and integrin expression in D2H and D2H, separately. Scale bar = 100 μm. **Supplemental Figure S7.** H₂ conditioned medium promotes collagen deposition *in vitro* in MSCs, fibroblasts and keratinocytes. **A.** Three positive markers in MSCs phenotype. **B.** Five negative markers in MSCs phenotype. **C.** α-SMA, Vimintin, and Col-1 expression in the HUCPF (fibroblast) between 66% H₂ and control groups 24 h after treatment. **D** and **E.** Col-1 deposit in the HaCat (keratinocyte) and HPF (fibroblast) cells between 66% H₂ and control groups 24 h after treatment. **Supplemental Figure S8.** 24-, 48-, and 72-h time points tissue cytokine profiling and four-color Flow Cytometry (FCM) of different targets showing quantification of CD3⁺, CD4⁺, and CD8⁺ T cells, as well as of Th₁, Th₂, Th₁₇ and Treg subgroups. **A.** FCM quantification of CD4⁺ and CD8⁺ cell distribution in all three groups. **B.** T-bet⁺/CD4⁺ T-cell distribution, double checked against IFN-γ⁺/CD4⁺ T-cell distribution. **C.** GATA3⁺/CD4⁺ T-cell distribution, double-checked against IL-4⁺/CD4⁺ T-cell distribution. **D.** IL-17A⁺/CD4⁺ T-cell distribution. **E.** CD25^{high}/CD127^{low} T-cell distribution. **F.** Example figures of gating strategy used in cytometry flow test, and the first four plots showed procedure of gating strategy from one of the typical samples in Th₁ subgroup cells analysis, the form showed the cell abundance during the gating strategy. **G.** Pro-inflammatory cytokine profile (TNF-α, IL-1β, and IL-6), Th₁₇-related cytokine (IL-17a and IFN-γ), and Anti-inflammatory cytokine IL-10 expression profile in all of the three groups at three time points. Data in **A-C** and **G** processed Two-way ANOVA test, and data in **D** and **E** processed unpaired t test. All data were plotted as Mean±SEM. * *P*-value < 0.05; ** *P*-value < 0.01; *** *P*-value < 0.001; no stars for *P*-value > 0.05. **Supplemental Figure S9.** High concentration of H₂ promoted early mussel and nerve repair. **A.** Left: Scheme of a mouse gastrocnemius strike model. Right: Timeline of animal experiments and daily H₂ treatment. **B.** Capture of the gastrocnemius strike area and blood perfusion 0-72 hours post-wounding in the 66% H₂ Control groups. **C.** & **D.** Quantification of diameter and blood perfusion of the gastrocnemius strike area between two groups. **E.** & **F.** Representative immunofluorescence images for NFH (green) nerve injury repair and axons maturation in dermal wounds of at day 3 and 11 post wounding. Data in **C** & **D** were processed unpaired T test. All of the data are plotted as Mean±SEM. * *P*-value < 0.05; ** *P*-value < 0.01; *** *P*-value < 0.001; no stars for *P*-value > 0.05; Scale bar = 100 μm. White dotted line in **E** & **F** indicates the boundary between the epithelium and dermis. Arrow in **E** & **F** indicates NFH⁺ cells. **Table S1.** List of primary and secondary antibodies used in experiments. **IHC** indicates immunocytochemistry, **IF** indicates immunofluorescence; **FC** indicates flow cytometry. **Table S2.** Gradient conditions for reversed phase C18 separation. **Table S3.** Gradient conditions for HILIC separation of polar metabolites. **Table S4.** DEGs annotation of all the 6 groups. **Table S5.** DEGs annotation of D1H vs D1C. **Table S6.** DEGs annotation of D2H vs D2C. **Table S7.** DEGs annotation of D3H vs D3C. **Table S8.** Raw data of nontargeted metabolomic analysis between D3H and D3C. **Table S9.** 12 metabolites identified through hydrophilic-product test between 66% H₂ and Control group. **Table S10.** Top 20 significant pathways discovered by nontargeted metabolomic analysis between the D3H and D3C groups.

Additional file 2: Movie S1. Live cell imaging of HPF cells under H₂ medium condition within 24 h. HPF cells stained by actin-GFP images were taken every one hour, and 0, 4, 8, 12, 16, 20 and 24 h images were collected to build the video. Bar indicates 1000 μ.

Additional file 3: Movie S2. Live cell imaging of HPF cells under normal condition within 24 h. HPF cells stained by actin-GFP images were taken every one hour, and 0, 4, 8, 12, 16, 20 and 24 h images were collected to build the video. Bar indicates 1000 μm.

Acknowledgements

We thank the Department of Hyperbaric Oxygen, Sixth Medical Center of PLA General Hospital, Beijing, China, for the generous help during our research.

Preprint version online

This manuscript has been posted online in Research Square as a preprint version since July 5th, 2022. The link of our preprint version is provided, which has reached 1849 views and 177 downloads by the time of submission. <https://doi.org/10.21203/rs.3.rs-1822552/v1>.

Authors' contributions

Xuemei Ma conceptualized the study and supervised the study, with assistance from Youbin Wang and Shuyi Pan. Pengxiang Zhao designed the experiments. Pengxiang Zhao, Zheng Dang, Mengyu Liu, Dazhi Guo, and Ruiliu Luo performed the animal modeling, administration and sampling work. Pengxiang Zhao, Zheng Dang, Mengyu Liu, Mingzi Zhang, Xujuan Zhang, and Fei Xie performed the experimental work and data analysis. Pengxiang Zhao wrote the manuscript. All authors read and approved the final manuscript.

Funding

This work was supported by the Military Logistics Key Open Research Projects (BHJ17L018) and National Natural Science Foundation of China (81602408).

Availability of data and materials

The datasets used and/or analyzed during the current study are available from the corresponding author on reasonable request.

Declarations

Ethics approval and consent to participate

Animal Experiment Committee of the Chinese People's Liberation Army (PLA) General Hospital and were carried out in accordance with the Regulations for the Administration of Affairs Concerning Experimental Animals (China) and the ARRIVE guidelines.

Consent for publication

Not applicable.

Competing interests

The authors declare that they have no competing interests.

Author details

¹Faculty of Environment and Life, Beijing University of Technology, Beijing 100124, People's Republic of China. ²Beijing Molecular Hydrogen Research Center, Beijing 100124, People's Republic of China. ³Beijing International Science and Technology Cooperation Base of Antiviral Drug, Beijing 100124, People's Republic of China. ⁴Department of Hyperbaric Oxygen, Sixth Medical Center of PLA General Hospital, Beijing 100048, People's Republic of China. ⁵Department of Plastic Surgery, Peking Union Medical College Hospital (Dongdan campus), No. 1 Shuaifuyuan Wangfujing Dongcheng District, Beijing 100730, People's Republic of China.

Received: 2 December 2022 Accepted: 26 February 2023

Published online: 28 March 2023

References

- Sun BK, Siprashvili Z, Khavari PA. Advances in skin grafting and treatment of cutaneous wounds. *Science*. 2014;346(6212):941–5.
- Clark RA. Fibrin and wound healing. *Ann N Y Acad Sci*. 2001;936(1):355–67.
- Eming SA, Martin P, Tomic-Canic M. Wound repair and regeneration: mechanisms, signaling, and translation. *Sci Transl Med*. 2014;6(265):265sr266.
- Coulombe PA. Wound epithelialization: accelerating the pace of discovery. *J Invest Dermatol*. 2003;121(2):219–30.
- Martin P. Wound healing—aiming for perfect skin regeneration. *Science*. 1997;276(5309):75–81.
- Shaw TJ, Martin P. Wound repair at a glance. *J Cell Sci*. 2009;122(18):3209–13.
- Gurtner GC, Werner S, Barrandon Y, Longaker MT. Wound repair and regeneration. *Nature*. 2008;453(7193):314.
- Schultz GS, Sibbald RG, Falanga V, Ayello EA, Dowsett C, Harding K, et al. Wound bed preparation: a systematic approach to wound management. *Wound Repair Regen*. 2003;11:51–528.
- Leaper DJ, Schultz G, Carville K, Fletcher J, Swanson T, Drake R. Extending the TIME concept: what have we learned in the past 10 years? *Int Wound J*. 2012;9:1–19.
- Lanza R, Langer R, Vacanti J. Principles of tissue engineering. Amsterdam: Elsevier, Academic press; 2007.
- Dekoninck S, Blanpain C. Stem cell dynamics, migration and plasticity during wound healing. *Nat Cell Biol*. 2019;21(1):18–24.
- Rousselle P, Montmasson M, Garnier C. Extracellular matrix contribution to skin wound re-epithelialization. *Matrix Biol*. 2019;75:12–26.
- Tumbar T, Guasch G, Greco V, Blanpain C, Lowry WE, Rendl M, et al. Defining the epithelial stem cell niche in skin. *Science*. 2004;303(5656):359–63.
- Ito M, Liu Y, Yang Z, Nguyen J, Liang F, Morris RJ, et al. Stem cells in the hair follicle bulge contribute to wound repair but not to homeostasis of the epidermis. *Nat Med*. 2005;11(12):1351.
- Levy V, Lindon C, Harfe BD, Morgan BA. Distinct stem cell populations regenerate the follicle and interfollicular epidermis. *Dev Cell*. 2005;9(6):855–61.
- Levy V, Lindon C, Zheng Y, Harfe BD, Morgan BA. Epidermal stem cells arise from the hair follicle after wounding. *FASEB J*. 2007;21(7):1358–66.
- Mascre G, Dekoninck S, Drogat B, Youssef KK, Brohée S, Sotiropoulou PA, et al. Distinct contribution of stem and progenitor cells to epidermal maintenance. *Nature*. 2012;489(7415):257.
- Li Y, Zhang J, Yue J, Gou X, Wu X. Epidermal stem cells in skin wound healing. *Adv Wound Care*. 2017;6(9):297–307.
- Yang R, Wang J, Chen X, Shi Y, Xie J. Epidermal stem cells in wound healing and regeneration. *Stem Cells Int*. 2020;2020. Article ID 9148310, 11 pages.
- Juhasz I, Murphy G, Yan H-C, Herlyn M, Albelda S. Regulation of extracellular matrix proteins and integrin cell substratum adhesion receptors on epithelium during cutaneous human wound healing in vivo. *Am J Pathol*. 1993;143(5):1458.
- Clark RA. The molecular and cellular biology of wound repair. New York: Springer Science & Business Media; 2013.
- Schultz GS, Davidson JM, Kirsner RS, Bornstein P, Herman IM. Dynamic reciprocity in the wound microenvironment. *Wound Repair Regen*. 2011;19(2):134–48.
- Gonzales KAU, Fuchs E. Skin and its regenerative powers: an alliance between stem cells and their niche. *Dev Cell*. 2017;43(4):387–401.
- Jimi S, Kimura M, De Francesco F, Riccio M, Hara S, Ohjimi H. Acceleration mechanisms of skin wound healing by autologous micrograft in mice. *Int J Mol Sci*. 2017;18(8):1675.
- Kaiser CA, Krieger M, Lodish H, Berk A. Molecular cell biology. San Francisco: WH Freeman; 2007.
- Lohmann N, Schirmer L, Atallah P, Wandel E, Ferrer RA, Werner C, et al. Glycosaminoglycan-based hydrogels capture inflammatory chemokines and rescue defective wound healing in mice. *Sci Transl Med*. 2017;9(386):eaai9044.
- Kuo Y-R, Wang C-T, Cheng J-T, Kao G-S, Chiang Y-C, Wang C-J. Adipose-derived stem cells accelerate diabetic wound healing through the induction of autocrine and paracrine effects. *Cell Transplant*. 2016;25(1):71–81.
- Kim SM, Kim YH, Jun YJ, Yoo G, Rhie JW. The effect of diabetes on the wound healing potential of adipose-tissue derived stem cells. *Int Wound J*. 2016;13:33–41.
- Barrientos S, Brem H, Stojadinovic O, Tomic-Canic M. Clinical application of growth factors and cytokines in wound healing. *Wound Repair Regen*. 2014;22(5):569–78.
- Rodrigues M, Kosaric N, Bonham CA, Gurtner GC. Wound healing: a cellular perspective. *Physiol Rev*. 2019;99(1):665–706.
- Cano Sanchez M, Lancel S, Boulanger E, Neviere R. Targeting oxidative stress and mitochondrial dysfunction in the treatment of impaired wound healing: a systematic review. *Antioxidants*. 2018;7(8):98.
- Ohsawa I, Ishikawa M, Takahashi K, Watanabe M, Nishimaki K, Yamagata K, et al. Hydrogen acts as a therapeutic antioxidant by selectively reducing cytotoxic oxygen radicals. *Nat Med*. 2007;13(6):688.
- Cai J, Kang Z, Liu WW, Luo X, Qiang S, Zhang JH, et al. Hydrogen therapy reduces apoptosis in neonatal hypoxia-ischemia rat model. *Neurosci Lett*. 2008;441(2):167–72.
- Liu Y-Q, Liu Y-F, Ma X-M, Xiao Y-D, Wang Y-B, Zhang M-Z, et al. Hydrogen-rich saline attenuates skin ischemia/reperfusion induced apoptosis via regulating Bax/Bcl-2 ratio and ASK-1/JNK pathway. *J Plast Reconstr Aesthet Surg*. 2015;68(7):e147–56.

35. Hirano S-i, Ichikawa Y, Sato B, Yamamoto H, Takefuji Y, Satoh F: Potential therapeutic applications of hydrogen in chronic inflammatory diseases: Possible inhibiting role on mitochondrial stress. *Int J Mol Sci.* 2021;22(5):2549.
36. Sano M, Tamura T: Hydrogen gas therapy: From preclinical studies to clinical trials. *Curr Pharm Des.* 2021;27(5):650–8.
37. Li Y, Shen C, Zhou X, Zhang J, Lai X, Zhang Y: Local treatment of hydrogen-rich saline promotes wound healing in vivo by inhibiting oxidative stress via Nrf-2/HO-1 pathway. *Oxid Med Cell Longev.* 2022;2022. Article ID 2949824, 13 pages.
38. Guo SX, Jin YY, Fang Q, You CG, Wang XG, Hu XL, et al: Beneficial effects of hydrogen-rich saline on early burn-wound progression in rats. *PLoS One.* 2015;10(4):e0124897.
39. Qiang L, Shinya K, Daigo M, Hiroshi T, Nobuhiko M: Hydrogen water intake via tube-feeding for patients with pressure ulcer and its reconstructive effects on normal human skin cells in vitro. *Med Gas Res.* 2013;3:1–17.
40. Wei F, Wang G, Tang L, Su H, Chen H, Liao W, et al: Hydrogen gas inhalation protects against cutaneous ischaemia/reperfusion injury in a mouse model of pressure ulcer. *J Cell Mol Med.* 2018;22(9):4243–52.
41. Zheng Y, Zhang Z, Wang T, Zhang J, Wu Z: Photodriven nanoreactor with a hydrogen-insulin double act repairs diabetic wounds through Nrf2 pathway activation. *Chem Eng J.* 2021;22:131800.
42. Chen H, Guo Y, Zhang Z, Mao W, Shen C, Xiong W, et al: Symbiotic algae–bacteria dressing for producing hydrogen to accelerate diabetic wound healing; 2021.
43. Watanabe S, Fujita M, Ishihara M, Tachibana S, Yamamoto Y, Kaji T, et al: Protective effect of inhalation of hydrogen gas on radiation-induced dermatitis and skin injury in rats. *J Radiat Res.* 2014;55(6):1107–13.
44. Zhu Q, Wu Y, Li Y, Chen Z, Wang L, Hao X, et al: Positive effects of hydrogen-water bathing in patients of psoriasis and parapsoriasis en plaques. *Entific Rep.* 2018;8(1):8051.
45. Tamaki N, Orihuela-Campos RC, Fukui M, Ito H-O: Hydrogen-rich water intake accelerates oral palatal wound healing via activation of the Nrf2/antioxidant defense pathways in a rat model. *Oxid Med Cell Longev.* 2016;2016. Article ID 5679040, 13 pages.
46. Kawasaki H, Guan J, Tamama K: Hydrogen gas treatment prolongs replicative lifespan of bone marrow multipotential stromal cells in vitro while preserving differentiation and paracrine potentials. *Biochem Biophys Res Commun.* 2010;397(3):608–13.
47. Zhang J, Xue X, Han X, Li Y, Lu L, Li D, et al: Hydrogen-rich water ameliorates total body irradiation-induced hematopoietic stem cell injury by reducing hydroxyl radical. *Oxid Med Cell Longev.* 2017;2017. Article ID 8241678, 16 pages.
48. Dunn L, Prosser HC, Tan JT, Vanags LZ, Ng MK, Bursill CA: Murine model of wound healing. *JoVE.* 2013;75:e50265.
49. Kobayashi M, Ota S, Terada S, Kawakami Y, Otsuka T, Fu FH, et al: The combined use of losartan and muscle-derived stem cells significantly improves the functional recovery of muscle in a young mouse model of contusion injuries. *Am J Sports Med.* 2016;44(12):3252–61.
50. Arnaoutova I, Kleinman HK: In vitro angiogenesis: endothelial cell tube formation on gelled basement membrane extract. *Nat Protoc.* 2010;5(4):628.
51. Adzavon YM, Zhao P, Ma J, Zhang X, Zhang X, Zhang M, et al: Macrophage migration inhibitory factor contributes to the pathogenesis of benign lymphoepithelial lesion of the lacrimal gland. *Cell Commun Signal.* 2018;16(1):70.
52. Fischer AH, Jacobson KA, Rose J, Zeller R: Hematoxylin and eosin staining of tissue and cell sections. *CSH Protoc.* 2008;2008(5):pdb.prot4986.
53. Dominici M, Le Blanc K, Mueller I, Slaper-Cortenbach I, Marini F, Krause D, et al: Minimal criteria for defining multipotent mesenchymal stromal cells. The International Society for Cellular Therapy position statement. *Cytotherapy.* 2006;8(4):315–7.
54. Rendell MS, Milliken BK, Finnegan MF, Finney DA, Healy JC: The skin blood flow response in wound healing. *Microvasc Res.* 1997;53(3):222–34.
55. Sen CK: Wound healing essentials: let there be oxygen. *Wound Repair Regen.* 2009;17(1):1–18.
56. Leaper D: Perfusion, oxygenation and warming. *Int Wound J.* 2007;4:4–8.
57. Krane SM: The importance of proline residues in the structure, stability and susceptibility to proteolytic degradation of collagens. *Amino Acids.* 2008;35(4):703.
58. Kirsner R, Eaglstein WH: The wound healing process. *Dermatol Clin.* 1993;11:629–40.
59. O'toole E: Extracellular matrix and keratinocyte migration. *Clin Exp Dermatol.* 2001;26(6):525–30.
60. Yoon S, Leube RE: Keratin intermediate filaments: intermediaries of epithelial cell migration. *Essays Biochem.* 2019;63(5):521–33.
61. Blanpain C, Fuchs E: Plasticity of epithelial stem cells in tissue regeneration. *Science.* 2014;344(6189):1242281. <https://doi.org/10.1126/science.1242281>.
62. Sánchez-Danés A, Hannezo E, Larsimont J-C, Liagre M, Youssef KK, Simons BD, et al: Defining the clonal dynamics leading to mouse skin tumour initiation. *Nature.* 2016;536(7616):298–303.
63. Henry G, Garner WL: Inflammatory mediators in wound healing. *Surg Clin.* 2003;83(3):483–507.
64. Zgheib C, Xu J, Liechty KW: Targeting inflammatory cytokines and extracellular matrix composition to promote wound regeneration. *Adv Wound Care.* 2014;3(4):344–55.
65. Wozniak D, Majewska-Szczepanik M, Kowalczyk P, Szczepanik M, Motyl S: Oral treatment with enrofloxacin early in life promotes Th2-mediated immune response in mice. *Pharmacol Rep.* 2016;68:44–50.
66. Ariotti S, Veldhoen M: Immunology: skin T cells switch identity to protect and heal. *Curr Biol.* 2019;29(6):R220–3.
67. Di Lullo GA, Sweeney SM, Korkko J, Ala-Kokko L, San Antonio JD: Mapping the ligand-binding sites and disease-associated mutations on the most abundant protein in the human, type I collagen. *J Biol Chem.* 2002;277(6):4223–31.
68. Aszodi A, Legate KR, Nakchbandi I, Fässler R: What mouse mutants teach us about extracellular matrix function. *Annu Rev Cell Dev Biol.* 2006;22:591–621.
69. Cuttle L, Nataatmadja M, Fraser JF, Kempf M, Kimble RM, Hayes MT: Collagen in the scarless fetal skin wound: Detection with Picrosirius-polarization. *Wound Repair Regen.* 2005;13(2):198–204.
70. Smith LT, Holbrook KA, Madri JA: Collagen types I, III, and V in human embryonic and fetal skin. *Am J Anat.* 1986;175(4):507–21.
71. Lovvorn Iii HN, Cheung DT, Nimni ME, Perelman N, Estes JM, Adzick NS: Relative distribution and crosslinking of collagen distinguish fetal from adult sheep wound repair. *J Pediatr Surg.* 1999;34(1):218–23.
72. Gurtner GC, Werner S, Barrandon Y, Longaker MT: Wound repair and regeneration. *Nature.* 2008;453(7193):314–21.
73. Ghosh K, Ren X-D, Shu XZ, Prestwich GD, Clark RA: Fibronectin functional domains coupled to hyaluronan stimulate adult human dermal fibroblast responses critical for wound healing. *Tissue Eng.* 2006;12(3):601–13.
74. Namazi MR, Fallahzadeh MK, Schwartz RA: Strategies for prevention of scars: what can we learn from fetal skin? *Int J Dermatol.* 2011;50(1):85–93.
75. Aumailley M: Laminins and interaction partners in the architecture of the basement membrane at the dermal-epidermal junction. *Exp Dermatol.* 2021;30(1):17–24.
76. Has C, Kern JS: Collagen XVII. *Dermatol Clin.* 2010;28(1):61–6.
77. Babu M: Collagen based dressings—a review. *Burns.* 2000;26(1):54–62.
78. Sharma S, Rai VK, Narang RK, Markandeywar TS: Collagen-based formulations for wound healing: a literature review. *Life Sci.* 2022;290:120096.
79. Pihlajaniemi T, Myllylä R, Kivirikko KI: Prolyl 4-hydroxylase and its role in collagen synthesis. *J Hepatol.* 1991;13:52–7.
80. Karna E, Szoka L, Huynh TYL, Palka JA: Proline-dependent regulation of collagen metabolism. *Cell Mol Life Sci.* 2020;77(10):1911–8.
81. Mihout F, Shweke N, Bigé N, Jouanneau C, Dussaule JC, Ronco P, et al: Asymmetric dimethylarginine (ADMA) induces chronic kidney disease through a mechanism involving collagen and TGF-β1 synthesis. *J Pathol.* 2011;223(1):37–45.
82. Gill SE, Parks WC: Metalloproteinases and their inhibitors: regulators of wound healing. *Int J Biochem Cell Biol.* 2008;40(6–7):1334–47.
83. Plikus MV, Gay DL, Treffeisen E, Wang A, Supapannachart RJ, Cotsarelis G: Epithelial stem cells and implications for wound repair. In: *Seminars in cell & developmental biology.* England: Elsevier; 2012. p. 946–53.
84. Dalton S: Linking the cell cycle to cell fate decisions. *Trends Cell Biol.* 2015;25(10):592–600.

85. Ito M, Liu Y, Yang Z, Nguyen J, Liang F, Morris RJ, et al. Stem cells in the hair follicle bulge contribute to wound repair but not to homeostasis of the epidermis. *Nat Med*. 2005;11(12):1351–4.
86. Blanpain C, Fuchs E. Epidermal homeostasis: a balancing act of stem cells in the skin. *Nat Rev Mol Cell Biol*. 2009;10(3):207.
87. Lin Z, Jin S, Chen J, Li Z, Lin Z, Tang L, et al. Murine interfollicular epidermal differentiation is gradualistic with GRHL3 controlling progression from stem to transition cell states. *Nat Commun*. 2020;11(1):1–15.
88. Snippert HJ, Haegerbarth A, Kasper M, Jaks V, van Es JH, Barker N, et al. Lgr6 marks stem cells in the hair follicle that generate all cell lineages of the skin. *Science*. 2010;327(5971):1385–9.
89. Bose A, Teh M-T, Mackenzie IC, Waseem A. Keratin k15 as a biomarker of epidermal stem cells. *Int J Mol Sci*. 2013;14(10):19385–98.
90. Abbas O, Richards JE, Yaar R, Mahalingam M. Stem cell markers (cytokeratin 15, cytokeratin 19 and p63) in in situ and invasive cutaneous epithelial lesions. *Mod Pathol*. 2011;24(1):90.
91. Tamai K, Yamazaki T, Chino T, Ishii M, Otsuru S, Kikuchi Y, et al. PDGFR α -positive cells in bone marrow are mobilized by high mobility group box 1 (HMGB1) to regenerate injured epithelia. *Proc Natl Acad Sci*. 2011;108(16):6609–14.
92. Li M, Ma J, Gao Y, Dong M, Zheng Z, Li Y, et al. Epithelial differentiation of human adipose-derived stem cells (hASCs) undergoing three-dimensional (3D) cultivation with collagen sponge scaffold (CSS) via an indirect co-culture strategy. *Stem Cell Res Ther*. 2020;11(1):1–16.
93. Shen M, Zhang H, Yu C, Wang F, Sun X. A review of experimental studies of hydrogen as a new therapeutic agent in emergency and critical care medicine. *Med Gas Res*. 2014;4(1):17.
94. Battin EE, Brumaghim JL. Antioxidant activity of sulfur and selenium: a review of reactive oxygen species scavenging, glutathione peroxidase, and metal-binding antioxidant mechanisms. *Cell Biochem Biophys*. 2009;55(1):1–23.
95. Antico Arciuch VG, Elguero ME, Poderoso JJ, Carreras MC. Mitochondrial regulation of cell cycle and proliferation. *Antioxid Redox Signal*. 2012;16(10):1150–80.
96. Da Silva AF, Mariotti FR, Máximo V, Campello S. Mitochondria dynamism: of shape, transport and cell migration. *Cell Mol Life Sci*. 2014;71(12):2313–24.
97. Zhang X, Zhang Z, Wei Y, Li M, Zhao P, Adzavon YM, Liu M, Zhang X, Xie F, Wang A: Mitochondria in higher plants possess H2 evolving activity which is closely related to complex I. *arXiv preprint arXiv:200102132* 2020.
98. Ma X, Zhang X, Xie F, Zhao P, Zhang Z, Yi Y. Bio-enzyme basis of hydrogen in biological system. *Curr Biotech*. 2020;10(1):15–22.
99. Zhang X, Xie F, Zhang Z, Adzavon YM, Su Z, Zhao Q, et al. Hydrogen evolution and absorption phenomena in the plasma membrane of *Vigna radiata* and *Capsicum annum*. *J Plant Growth Regul*. 2023;42(1):249–59.
100. Zhang X, Yi Y, Xie F, Zhang Z, Ma S, Zhao P, et al. Study on effect of hydrogen on excitatory conduction in rats. *Curr Biotechnol*. 2020;10(4):393–9.
101. Jin Z, Zhao P, Gong W, Ding W, He Q. Fe-porphyrin: a redox-related biosensor of hydrogen molecule. *Nano Res*. 2023;16:2020–5.
102. Yi Y, Zhang X, Guo B, Xie F, Zhang Z, Ma S, et al. Effect of hydrogen on horseradish peroxidase activity and its mechanism. *Chin J Biochem Mol Biol*. 2020;36(7):811–9.
103. Zhao P-X, Luo R-L, Dang Z, Wang Y-B, Zhang X-J, Liu Z-Y, et al. Effect of hydrogen intervention on refractory wounds after radiotherapy: A case report. *World J Clin Cases*. 2022;10(21):7545.
104. Yu S, Li G, Zhao P, Cheng Q, He Q, Ma D, et al. NIR-laser-controlled hydrogen-releasing pdh nanohydride for synergistic hydrogen-photo-thermal antibacterial and wound-healing therapies. *Adv Funct Mater*. 2019;29(50):1905697.

Publisher's Note

Springer Nature remains neutral with regard to jurisdictional claims in published maps and institutional affiliations.

Ready to submit your research? Choose BMC and benefit from:

- fast, convenient online submission
- thorough peer review by experienced researchers in your field
- rapid publication on acceptance
- support for research data, including large and complex data types
- gold Open Access which fosters wider collaboration and increased citations
- maximum visibility for your research: over 100M website views per year

At BMC, research is always in progress.

Learn more biomedcentral.com/submissions

